nature cancer

Article

https://doi.org/10.1038/s43018-025-00905-6

FLASH radiation reprograms lipid metabolism and macrophage immunity and sensitizes medulloblastoma to CAR-T cell therapy

Received: 22 November 2023

Accepted: 7 January 2025

Published online: 05 February 2025

Check for updates

A list of authors and their affiliations appears at the end of the paper

FLASH radiotherapy holds promise for treating solid tumors given the potential lower toxicity in normal tissues but its therapeutic effects on tumor immunity remain largely unknown. Using a genetically engineered mouse model of medulloblastoma, we show that FLASH radiation stimulates proinflammatory polarization in tumor macrophages. Single-cell transcriptome analysis shows that FLASH proton beam radiation skews macrophages toward proinflammatory phenotypes and increases T cell infiltration. Furthermore, FLASH radiation reduces peroxisome proliferator-activated receptor-γ (PPARγ) and arginase 1 expression and inhibits immunosuppressive macrophage polarization under stimulus-inducible conditions. Mechanistically, FLASH radiation abrogates lipid oxidase expression and oxidized low-density lipid generation to reduce PPARγ activity, while standard radiation induces reactive oxygen species-dependent PPARγ activation in macrophages. Notably, FLASH radiotherapy improves infiltration and activation of chimeric antigen receptor (CAR) T cells and sensitizes medulloblastoma to GD2 CAR-T cell therapy. Thus, FLASH radiotherapy reprograms macrophage lipid metabolism to reverse tumor immunosuppression. Combination FLASH–CAR radioimmunotherapy may offer exciting opportunities for solid tumor treatment.

Childhood cancer is a leading cause of death in children. Among these, medulloblastoma (MB) is the most frequently occurring malignant brain tumor in children[1]. Despite aggressive treatments involving surgical resection, standard ionizing irradiation and chemotherapy, the prognosis for persons with high-risk MB remains poor[2]. Immunotherapy holds great promise in improving brain cancer outcomes; however, current immunotherapy methods, which primarily focus on T cell use or activation, face notable challenges in treating brain tumors. These challenges arise mainly from an immune-hostile microenvironment that hinders T cell infiltration and activation within the tumors. Because of their immunologically inert characteristics, most brain tumors display resistance to T cell-based immunotherapies, including checkpoint blockade and adoptive cell transfer using chimeric antigen receptor (CAR)-modified T cells[3–6]. In brain tumors, the primary source of immunosuppression originates from tumor-associated myeloid cells, particularly macrophages (Mϕs) that constitute the majority of non-neoplastic cells[7,8]. Tumor-associated Mϕs usually undergo alternative M2 polarization and secrete immunosuppressive factors, such as interleukin 10 (IL-10), transforming growth factor-β (TGFβ) and arginase 1, to induce tumor immunosuppression[9–15]. Consequently, the development of promising approaches that reprogram Mϕs to overcome tumor resistance to immunotherapy is critically needed for the treatment of pediatric brain tumors.

Radiotherapy (RT) has been generally considered as an 'in situ vaccination' treatment to stimulate antitumor immunity as it causes tumor cell lysis to release tumor-specific antigens that can be recognized

e-mail: david.kirsch@uhn.ca; gongy@pennmedicine.upenn.edu; fanyi@upenn.edu

by immune cells[16]. However, the impact of standard radiation on Mϕ phenotypes appears to be conflicting, depending on dose, location and cancer types[17–23], posing challenges for combining immunotherapy with standard RT. Notably, growing evidence suggests that ultrahigh-dose-rate delivery of radiation (that is, FLASH RT at a dose rate of ≥40 Gy s^{-1}) can improve the therapeutic ratio of radiation and reduce normal tissue toxicity[24–28]. Considering the crucial importance of preserving normal brain functions and neurocognitive benefits[29], FLASH RT holds great promise for treating the pediatric population with brain tumors. Here, we sought to investigate the therapeutic effects of FLASH RT on MB immunity and the underlying regulatory mechanism through single-cell and bulk transcriptome analyses. Our data show that FLASH RT stimulates proinflammatory Mϕ phenotypes in vitro and in vivo through regulating reactive oxygen species (ROS)-dependent peroxisome proliferator-activated receptor-γ (PPARγ) activation. Strikingly, FLASH RT robustly improves CAR-T cell infiltration into MB tumors. Our study suggests that combined FLASH and CAR-T radioimmunotherapy is a promising strategy for treating pediatric brain tumors.

Results

Standard and FLASH RT improves survival in MB-bearing mice

To explore the effects of radiation in MB, we took advantage of a genetically engineered mouse MB model, based on Math1-Cre-driven specific overexpression of Smo^{W539L} (that is, SmoM2) in cerebellar granule cell neuron precursors in the hind brain (Fig. 1a). This model recapitulates the key features of the human sonic hedgehog type of MB, the most common subtype in young children under 3 years of age. Using a small animal radiation research platform incorporating high-resolution computed tomography, we were able to stereotactically deliver proton beams into mouse MB tumors at a standard (0.7 Gy s^{-1}) or FLASH (~100 Gy s^{-1}) dose rate (Fig. 1a). Our results show that 10-Gy FLASH and standard RT significantly ($P < 0.05$) and equivalently extended animal survival by ~50%, providing comparable tumor control (Fig. 1b).

FLASH RT stimulates antitumor immunity in MB

We next analyzed the impact of RT on global transcriptome in different cell populations using single-cell RNA sequencing (RNAseq). Nonlinear dimensionality reduction by uniform manifold approximation and projection (UMAP) analysis of the whole transcriptome gene signature assigned the single cells into several transcriptionally distinct cell clusters, including tumor cells, endothelial cells, oligodendrocytes/astrocytes and microglia/leukocytes (Fig. 1c,d). Interestingly, transcriptome analysis revealed that the top genes upregulated in FLASH-irradiated tumors included CD8a, a marker of cytotoxic T cells, and CD80 and CD86, two costimulatory receptors that are critical for T cell-activating responses in myeloid cells (Fig. 1e), suggesting a potential antitumor proinflammatory effect by FLASH RT. Consistent with these findings, analysis of $CD11b^+$ myeloid cells showed that FLASH RT induced more robust expression of CD86 and CD80 and less expression of CD206, a surface marker of immunosuppressive myeloid cells (Fig. 1f). Further analysis of these $CD11b^+$ myeloid cells identified *Arg1* (arginase 1) among the most downregulated genes in FLASH-irradiated tumors (Fig. 1g,h). *Arg1* is a known immunosuppressant that inhibits T cell activity in tumors[30]. To validate these results, we performed flow cytometry analysis of tumor-derived single-cell suspensions. Our results showed that FLASH enhanced the infiltration of total $CD45^+$ hematopoietic cells (Fig. 1i and Extended Data Fig. 1a). Interestingly, FLASH RT increased the proinflammatory M1-like $CD86^+$ Mϕ population (Fig. 1j) and decreased anti-inflammatory M2-like $CD206^+$ Mϕ population (Fig. 1k) compared to the no RT condition, while standard RT did not robustly affect these Mϕ populations, suggesting that FLASH RT stimulates a more proinflammatory response in tumor Mϕs. In addition, flow cytometry analysis showed that FLASH or standard RT did not affect the population of total Mϕs or total and M1-like microglia cells (Extended Data Fig. 1b,c) and only FLASH RT reduced the population of M2-like microglia cells (Extended Data Fig. 1d). In accordance with these findings, FLASH RT enhanced the infiltration of $CD3^+$ T cells into the tumors (Fig. 1l). Moreover, FLASH RT increased the percentage of $CD8^+$ T cells in total T cells and the ratio of $CD8^+$ to $CD4^+$ T cells (Fig. 1m–o). FLASH and standard RT slightly yet insignificantly ($P > 0.05$) increased the infiltration of natural killer (NK) cells (Extended Data Fig. 1e). Taken together, these findings indicate that FLASH RT induces more favorable immune responses in MB compared to standard RT.

FLASH RT induces proinflammatory Mϕ phenotypes in vitro

We next investigated the effects of radiation on Mϕ polarization, a key cellular process that regulates Mϕ function and immunosuppression. Mouse bone marrow (BM)-derived Mϕs were irradiated by a 5-Gy standard and FLASH proton beam, followed by M1-like and M2-like induction with lipopolysaccharide (LPS) and IL-4, respectively (Fig. 2a). Interestingly, FLASH RT enhanced the population of $CD80^+$ proinflammatory Mϕs under the M1 condition (Fig. 2b). Reverse transcription (RT)–PCR analysis verified that FLASH RT enhanced the expression of proinflammatory IL-1β, while standard RT reduced its expression (Fig. 2c). Similar results were observed in irradiated human peripheral blood mononuclear cell (PBMC)-derived Mϕs (Extended Data Fig. 2). In accordance with these data, ELISA assays showed that FLASH RT but not standard RT enhanced the expression of proinflammatory cytokines including IL-1β and tumor necrosis factor (TNF) in these M1-like Mϕs (Fig. 2d,e). Furthermore, FLASH or standard RT did not significantly ($P > 0.05$) affect the population of anti-inflammatory $CD206^+$ Mϕs (Fig. 2f). However, FLASH but not standard RT reduced the expression of immunosuppressive arginase 1 (Fig. 2g). To test the effect of RT on Mϕ effector functions, control or irradiated Mϕs were incubated with human T cells, followed by flow cytometry analysis for T cell proliferation and activation. Our data show that IL-4-treated M2-like Mϕs inhibited T cell proliferation and expression of CD25, a maker of T cell activation (Extended Data Fig. 3). Importantly, FLASH RT but not standard RT rescued T cell proliferation (Extended Data Fig. 3a) and CD25 expression (Extended Data Fig. 3b) in the T cells incubated with these Mϕs. Together, these findings suggest that FLASH RT stimulates Mϕs toward proinflammatory M1 polarization and leads to T cell activation.

FLASH RT induces less PPAR γ expression and Mϕ suppression

To investigate the molecular mechanism by which FLASH and standard radiation modulate Mϕ function, we performed bulk RNAseq analysis of irradiated Mϕs under control or M1-like or M2-like condition. Our transcriptome analysis showed that LPS and IL-4 markedly switched global expression profile under unirradiated conditions (Fig. 3a). LPS robustly upregulated expression of CD86, while IL-4 enhanced expression of CD206 (*Mrc1*) and arginase 1 (*Arg1*) (Fig. 3b). Strikingly, radiation, particularly by standard RT, abrogated the transcriptome shift induced by LPS and IL-4 (Fig. 3a). Consistent with these findings, FLASH and standard RT seemed to evoke different immune responses, as FLASH RT induced less expression of immunosuppression-associated genes including *Mrc1* and *Arg1* and also more expression of immunostimulation-associated genes, including *Cd86*, *Il1b* (IL-1β) and *Tnf* (TNF), particularly in the M1-stimulatory condition (Fig. 3c). In accordance with our results from in vitro flow cytometry and RT–PCR analyses (Fig. 2), these findings collectively suggest that FLASH RT may cause a transcriptomic change toward a more proinflammatory and less anti-inflammatory status.

We explored the potential transcriptional regulation of Mϕ functions in these settings. We initially analyzed the expression of transcription factors (TFs) that are known as regulators of immunosuppressive M2 Mϕ polarization, including PPAR, Spi1, Cebp, Stat6, Klf4, Irf8, Fos, Jun and hypoxia-inducible factors HIF1α and HIF2β (*Epas1*). Notably, PPARγ was identified as the most robustly downregulated and upregulated factor by LPS and IL-4, respectively, in our system, which led us

https://doi.org/10.1038/s43018-025-00905-6

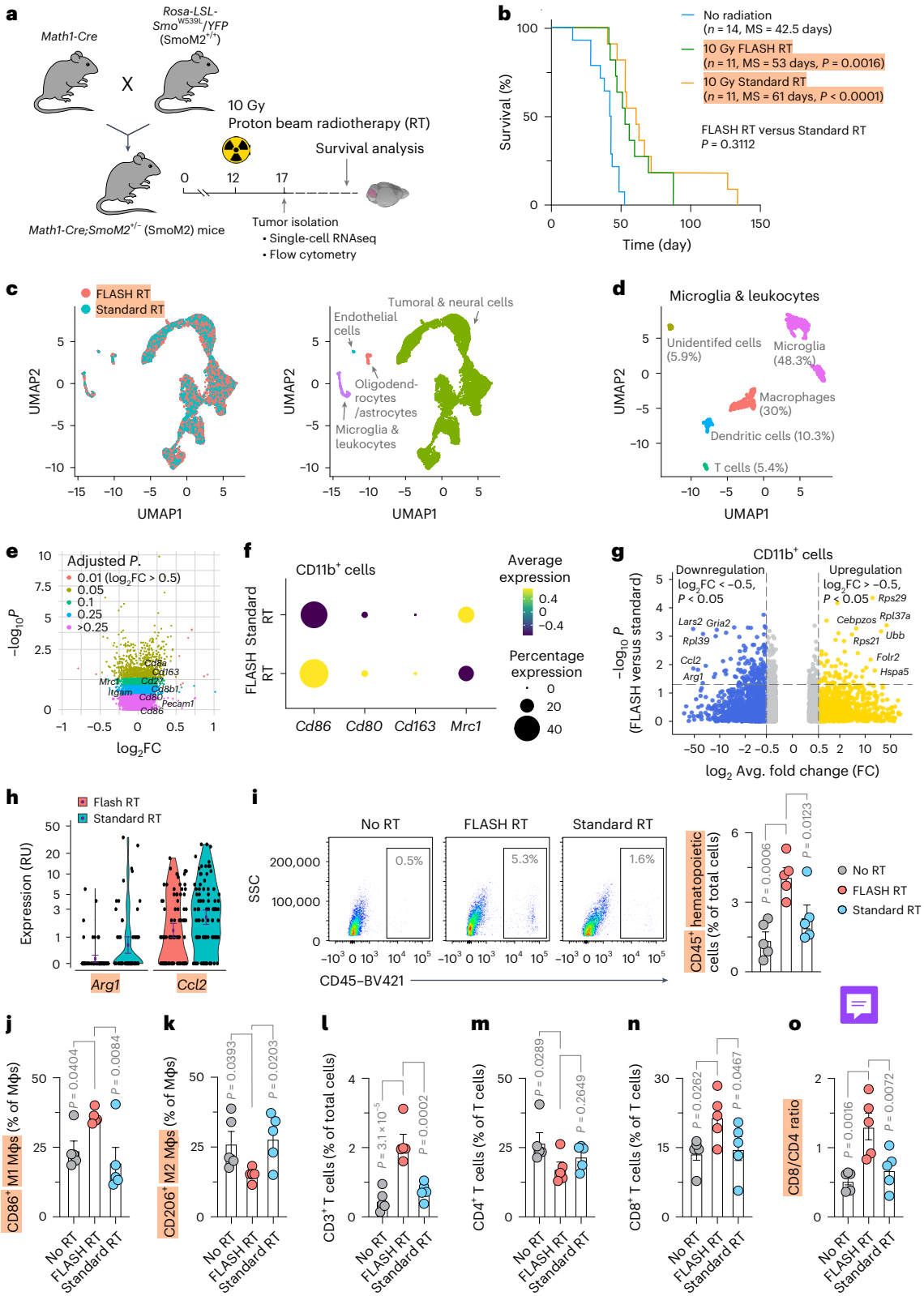

Fig. 1 | FLASH RT shows antitumor effects and skews Mϕs toward a proinflammatory phenotypes in mouse MB. MB was genetically engineered in SmoM2 mice, followed by irradiation with FLASH or standard proton beam. **a**, Experimental procedure. **b**, After irradiation with a 10-Gy proton beam, animal survival was monitored ($n = 11$–14 mice; specific n value of each group listed in the figure). Statistical analysis by log-rank test. **c**–**h**, Single-cell RNAseq analysis (pooled from $n = 3$ mice for each group). **c**, UMAP analysis of transcriptome gene signature in all tumor-derived cells. Left, integration of RNAseq data from samples irradiated with FLASH or standard proton beam. Right, distribution of cell clusters. **d**, UMAP analysis of transcriptome gene signature in microglia and leukocytes. **e**, Top regulated genes in microglia and leukocytes. FC, fold change. **f**, CD86, CD80, CD163 and CD206 (*Mrc1*) expression in CD11b$^+$ myeloid cells. **g**, Top altered genes in CD11b$^+$ myeloid cells. **h**, Arginase 1 (*Arg1*) and MCP1 (*Ccl2*) expression in CD11b$^+$ myeloid cells. **i**–**o**, Flow cytometry analysis for CD45$^+$ hematopoietic cells (**i**), CD86$^+$ M1-like Mϕs (**j**) and CD206$^+$ M2-like Mϕs (**k**) in CD11b$^+$F4/80$^+$ Mϕs, CD45$^+$CD3$^+$ T cells in total cells (**l**) and CD4$^+$ (**m**) and CD8$^+$ (**n**) T cells in CD45$^+$CD3$^+$ T cells and ratio of CD8$^+$/CD4$^+$ T cells (**o**) ($n = 5$ mice, mean ± s.e.m.). Statistical analysis by one-way ANOVA. **i**, Left, representative cell sortings. Right, quantified results.

https://doi.org/10.1038/s43018-025-00905-6

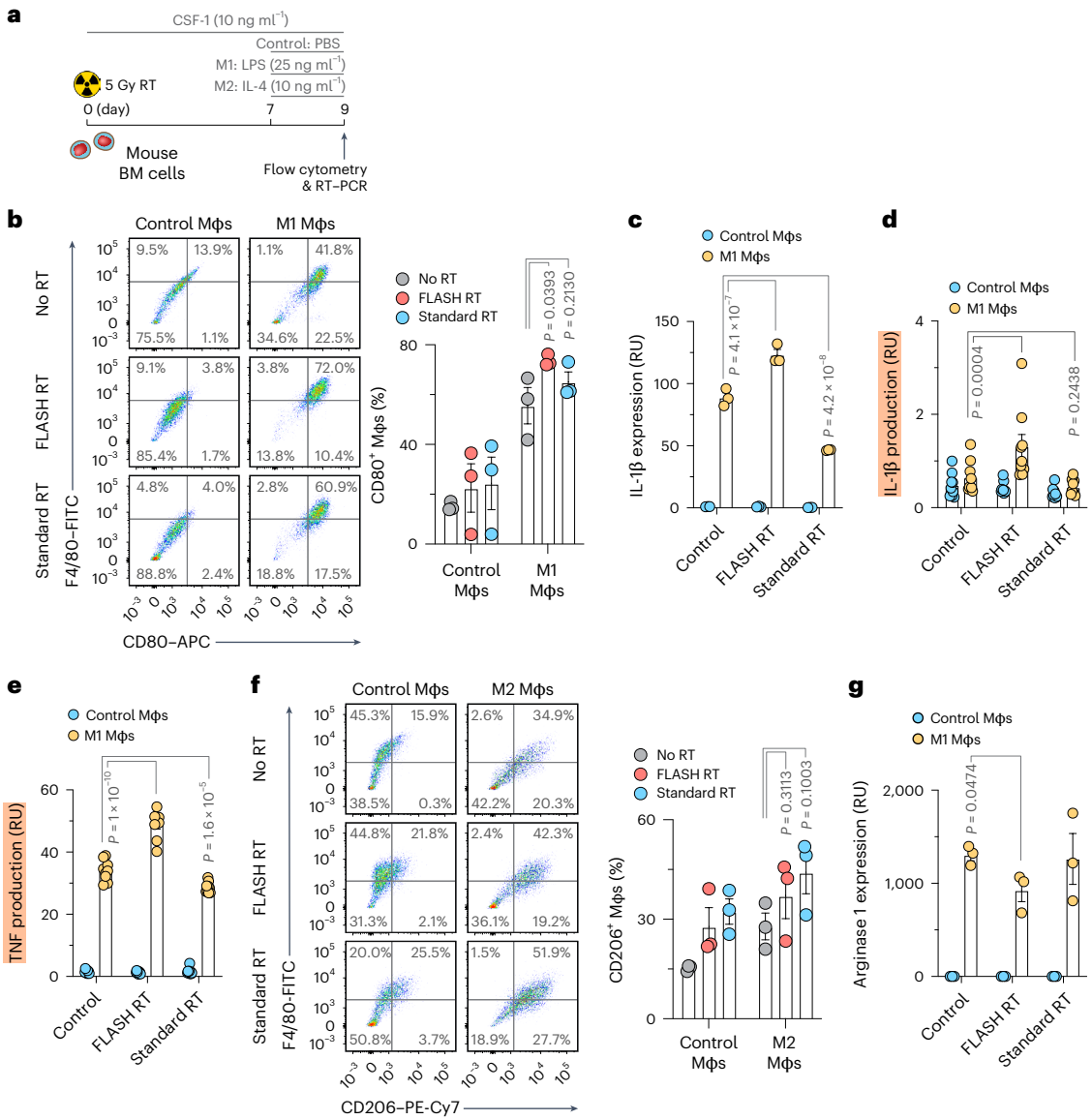

Fig. 2 | FLASH radiation stimulates the capacity for stimulus-dependent proinflammatory polarization in Mφs. Mouse BM-derived Mφs were irradiated with FLASH or standard proton beam, followed by treatment with LPS or IL-4. **a**, Experimental procedure. **b**–**e**, After treatment with LPS, cells were analyzed by flow cytometry (**b**), RT–PCR (**c**) or ELISA (**d**,**e**). **b**, Left, representative cell sortings. Right, quantified results ($n = 3$ mice, mean ± s.e.m.). **c**, Quantified results of RT–PCR ($n = 3$ mice, mean ± s.e.m.). **d**, ELISA results for IL-1β expression ($n = 9$ mice, mean ± s.e.m.). **e**, ELISA results for TNF expression ($n = 9$ mice, mean ± s.e.m.). **b**–**e**, Statistical analysis by one-way ANOVA. **f**,**g**, After treatment with IL-4, cells were analyzed by flow cytometry (**f**) and RT–PCR (**g**). **f**, Left, representative cell sortings. Right, quantified results ($n = 3$ mice, mean ± s.e.m.). Statistical analysis by one-way ANOVA. **g**, Quantified results of RT–PCR ($n = 3$ mice, mean ± s.e.m.). Statistical analysis by two-tailed Student's *t*-test.

to focus our next study on PPARγ (Fig. 3d). Compared to standard RT (+51.1%, versus unirradiated cells), FLASH RT induced substantially less expression of PPARγ (+1.8%, versus unirradiated cells) but not PPARα or PPARδ in Mφs under the M1 condition (Fig. 3e). Likewise, FLASH RT inhibited M2 condition-inducible expression of arginase 1 in Mφs (Fig. 3f). Considering a well-established role of PPARγ and arginase 1 for immunosuppressive polarization of tumor Mφs[31], these findings suggest that FLASH RT may inhibit PPARγ expression to drive less immune-inhibitory and more immune-stimulative phenotypes in Mφs.

FLASH RT inhibits oxidized low-density lipoprotein (oxLDL) generation to reduce PPARγ activity

To define the mechanism underlying FLASH RT-induced down-regulation of PPARγ, we initially tested its effects on ROS generation. Our results showed that FLASH RT did not induce a detectable increase in ROS production in mouse Mφs, while standard RT evoked a time-dependent ROS generation, peaking at 12 h after irradiation (Fig. 4a). Consistent with this result, FLASH RT induced less ROS generation in human PBMC-derived Mφs compared to standard RT (Extended Data Fig. 4a). Moreover, FLASH RT inhibited PPARγ activity but standard RT increased its activity in mouse Mφs (Fig. 4b). Similar results were observed in irradiated human Mφs (Extended Data Fig. 4b). Importantly, pretreatment of Mφs with ROS scavenger TEMPO abrogated standard RT-induced PPARγ activation (Fig. 4c), indicating that standard RT stimulates PPARγ activation through ROS. Likewise, scavenging ROS reduced arginase 1 expression in both nonirradiated and irradiated cells, suggesting a requisite role for ROS in arginase 1 expression (Fig. 4d). Together, these findings suggest that FLASH RT does not affect ROS production but inhibits PPARγ activity and standard RT stimulates ROS-dependent PPARγ activation and arginase 1 expression.

https://doi.org/10.1038/s43018-025-00905-6

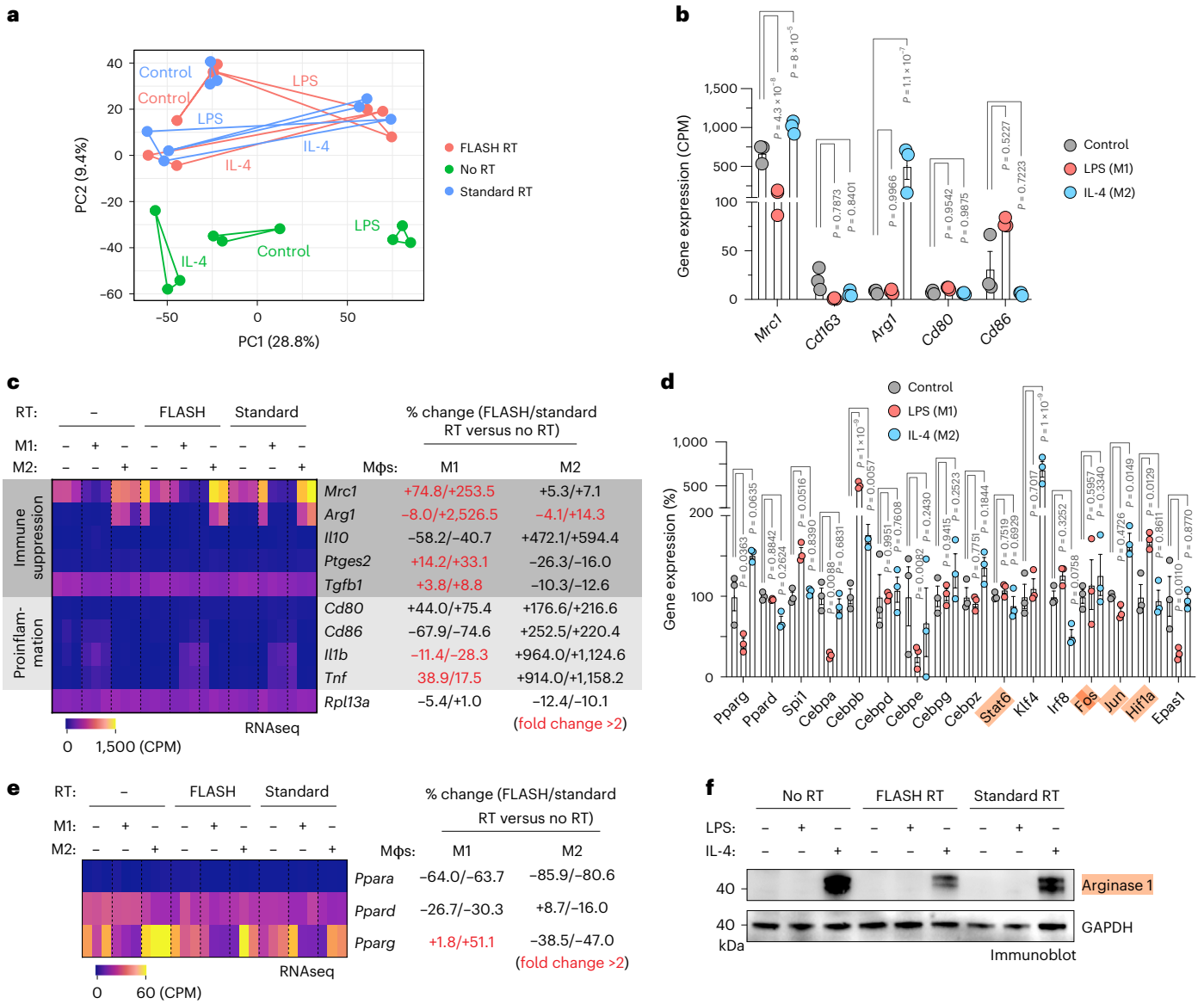

Fig. 3 | FLASH radiation induces less PPARγ expression and immunosuppressive phenotypes in Mϕs. Mouse BM-derived Mϕs were irradiated with 5-Gy FLASH or standard proton beam, followed by treated with LPS (M1) or IL-4 (M2). **a**–**e**, RNA was extracted and analyzed by RNAseq ($n = 3$ samples per group, pooled from three mice). **a**, Principal component analysis of all of the mapped genes. **b**, Expression of M1 and M2 marker genes in unirradiated Mϕs treated with or without LPS or IL-4 (mean ± s.e.m.). Statistical analysis by two-way ANOVA. **c**, Expression of immunosuppression-associated and proinflammation-associated genes in irradiated M1 or M2 Mϕs. Left, heat map of gene expression. Right, quantified changes over unirradiated cells (average percentage change). **d**, Expression of M2 polarization-associated TFs in unirradiated Mϕs treated with or without LPS or IL-4 (mean ± s.e.m.). Statistical analysis by one-way ANOVA. **e**, Expression of PPAR TFs in irradiated control, M1 Mϕs or M2 Mϕs. Left, heat map of gene expression. Right, quantified changes over unirradiated cells (average percentage change). **f**, Treated cells were analyzed by immunoblot. This experiment was repeated independently twice with similar results.

We next explored a potential role of oxLDL that contains oxidized lipids known to activate PPARγ[32,33]. Our data showed that FLASH RT inhibited oxLDL generation but standard RT enhanced it in mouse Mϕs (Fig. 4e). Similar results were observed in irradiated human Mϕs (Extended Data Fig. 4c). Production of oxLDL proceeds through ROS-mediated direct reaction and lipid oxidases including nicotinamide adenine dinucleotide phosphate oxidase (*Nox*), lipoxygenase (*Lox*) and myeloperoxidase (*Mpo*). Notably, both FLASH and standard RT markedly inhibited Mϕ expression of two major lipid oxidases, Alox12 and Mpo, as well as Alox5 to a lesser extent, as revealed by RNAseq analysis (Fig. 4f). RT–PCR analysis confirmed that FLASH and standard RT abrogated *Mpo* mRNA expression (Fig. 4g). This is likely because of a global altered activation of multiple TFs (Extended Data Fig. 5). Furthermore, pretreatment of Mϕs with ROS scavenger TEMPO inhibited standard RT-stimulated oxLDL production (Fig. 4h). These findings collectively suggest that FLASH radiation may reduce PPARγ activity through down-regulation of oxidase expression, while standard radiation may enhance PPARγ activation through ROS in Mϕs.

FLASH RT sensitizes tumors to GD2 CAR-T cell therapy

Because FLASH RT stimulates proinflammatory polarization in Mϕs in vitro and in vivo (Figs. 1–3) and enhances T cell infiltration into MB tumors in vivo (Fig. 1), we hypothesize that FLASH RT may sensitize brain tumors to T cell-based immunotherapy. To test this hypothesis, we aimed to develop immunotherapy using CAR-engineered mouse T cells that specifically target GD2, a well-known target for brain tumors[34,35].

https://doi.org/10.1038/s43018-025-00905-6

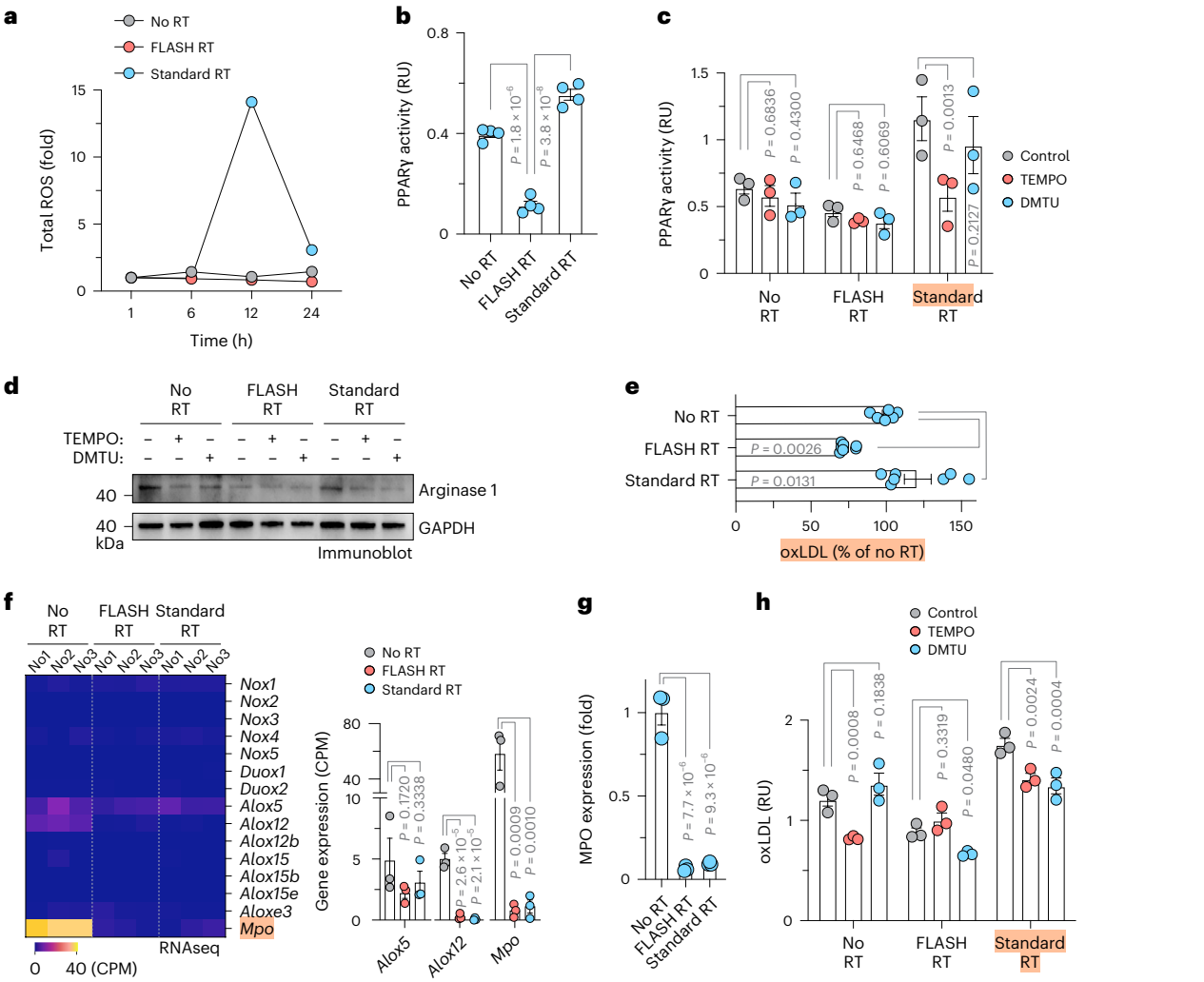

Fig. 4 | FLASH radiation inhibits oxidase expression and oxLDL generation to reduce PPARγ activity and arginase 1 expression, while standard radiation induces redox-dependent PPARγ activation and arginase 1 expression in Mϕs. a,**b**, Mouse BM-derived Mϕs were irradiated with 5-Gy FLASH or standard proton beam. **a**, Total ROS were analyzed at different times after irradiation (mean ± s.e.m., $n = 4$ mice). **b**, PPARγ activity was measured 24 h after radiation (mean ± s.e.m., $n = 4$ mice). Statistical analysis by one-way ANOVA. **c**,**d**, Mouse Mϕs were treated with TEMPO or DMTU, followed by FLASH or standard irradiation. **c**, PPARγ activity was measured 24 h after radiation (mean ± s.e.m., $n = 4$ mice). Statistical analysis by two-way ANOVA. **d**, Cell lysate was immunoblotted. This experiment was repeated independently twice with similar results. **e**–**g**, Mouse Mϕs were irradiated with 5-Gy FLASH or standard radiation. **e**, Cell lysates were subject to oxLDL analysis (mean ± s.e.m., $n = 7$ mice, pooled from two experiments). Statistical analysis by one-way ANOVA. **f**, RNA was extracted and analyzed by RNAseq ($n = 3$ samples, pooled from three mice; total of 27 mice). Left, heat map of oxidase gene expression. Right, quantified results. Statistical analysis by two-way ANOVA. **g**, RNA was extracted and analyzed by RT–PCR (mean ± s.e.m., $n = 3$ mice). Statistical analysis by one-way ANOVA. **h**, Mouse BM-derived Mϕs were treated with TEMPO or DMTU, followed by FLASH or standard radiation. Cell lysates were subjected to oxLDL analysis (mean ± s.e.m., $n = 3$ mice). Statistical analysis by one-way ANOVA.

To validate the expression of this target, we performed immunofluorescence and flow cytometry analyses of the tumors derived from our genetically engineered MB model. Tissue immunofluorescence analysis of mouse normal brain and MB tumors verified that GD2 was specifically and robustly expressed in MB tumors (Fig. 5a), which was further validated by flow cytometry analysis showing more than 60% of tumor-derived cells were GD2$^+$ (Fig. 5b), suggesting that GD2 is a vital and selective therapeutic target for MB. In addition, using a retrovirus-mediated murine CAR-T system we previously developed[36,37], we generated murine GD2 CAR-T cells with >40% CAR$^+$ T cells (Fig. 5c). An in vitro killing assay with tumor cells indicated that these CAR-T cells could directly induce cytotoxicity in GD2$^+$ mouse brain tumor cells in vitro (Fig. 5d). We investigated the effects of GD2 CAR-T cell monotherapy on animal survival in MB-bearing mice. MB was genetically induced in mice, followed by treatment with GD2 CAR-T cells injected intravenously (Fig. 5e). Unexpectedly, GD2 CAR-T cell therapy did not improve animal survival (Fig. 5f), likely because of no detectable tumor infiltration by CAR-T cells after infusion (Fig. 5g).

To test the effects of FLASH RT on CAR-T cell infiltration and animal survival, MB-bearing mice were treated by standard and FLASH RT, followed by T cell therapy with GD2 CAR or control single-chain variable fragment (scFV)-free CAR-T cells 5 days after the irradiation (Fig. 6a). Our data showed that combination treatment with FLASH RT plus GD2 CAR-T cells substantially extended animal survival (+27.5 days median, $P < 0.001$, compared to FLASH RT plus control CAR-T cells), while combination treatment with standard RT plus GD2 CAR-T cells moderately extended animal survival (+11.0 days median, $P < 0.001$, compared to standard RT plus control CAR-T cells) (Fig. 6b). Of note, 70% of the mice that received FLASH RT plus GD2 CAR-T combination therapy remained alive, whereas all mice in other groups died 83 days after tumor induction (Fig. 6b). In addition, we tested the effects of the combination therapy in a syngeneic glioma mouse model (Extended Data Fig. 6a).

https://doi.org/10.1038/s43018-025-00905-6

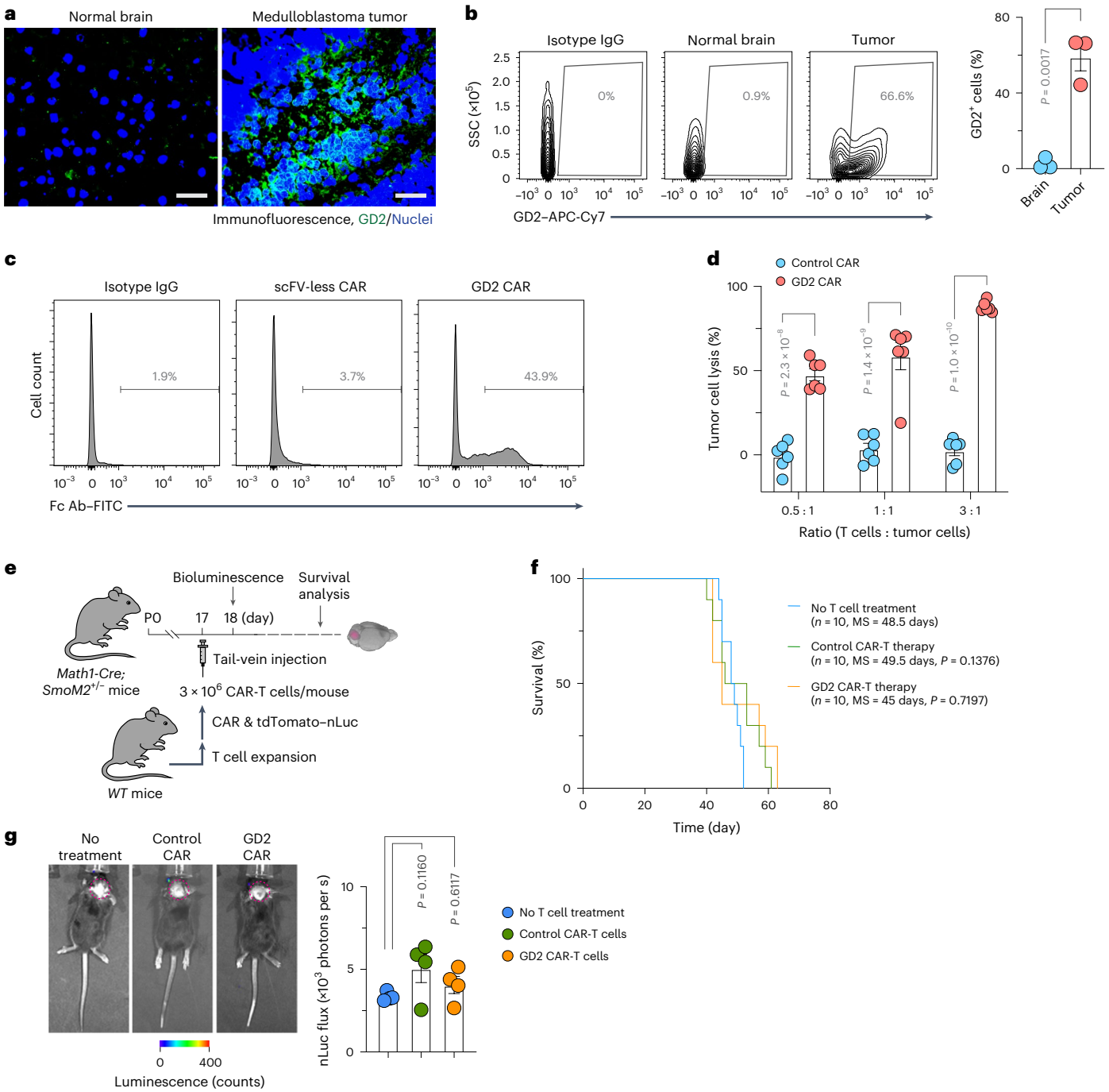

Fig. 5 | GD2 CAR-T cells show robust activity in vitro but minimal therapeutic efficacy in vivo. a,**b**, Normal brain and tumor tissues were excised from WT and SmoM2 mice. **a**, Tissue sections were immunostained with anti-GD2 antibody ($n = 4$ mice). Representative images are shown. Scale bars, 50 µm. **b**, Tissue-derived single-cell suspensions were immunostained and analyzed by flow cytometry. Left, representative sortings. Right, quantified results ($n = 3$ mice, mean ± s.e.m.). Statistical analysis by two-tailed Student's *t*-test. **c**–**g**, GD2 CAR-T therapy in mice. **c**, Preparation of CAR-T cells. Mouse T cells were retrovirally transduced to express control or GD2 CAR. Representative sortings are shown, **d**, Mouse tumor cells were isolated from MB tumors and incubated with control or GD2 mouse CAR-T cells, followed by cell lysis assay ($n = 6$ assays, mean ± s.e.m.). Statistical analysis by two-way ANOVA. **e**–**g**, SmoM2 mice were treated with or without control or GD2 CAR-T cells. **e**, Experimental procedures. **f**, Animal survival was monitored. Statistical analysis by log-rank test. **g**, Mice were imaged by bioluminescence. Left, representative images. Dashed circles indicate the brain area. Right, quantified luminescence signals in the brain area ($n = 4$ mice, mean ± s.e.m.). Statistical analysis by one-way ANOVA.

Our data showed that FLASH RT monotherapy alone induced a robust therapeutic effect (+29.5 days median, $P < 0.0001$, compared to control nonirradiated mice), while standard RT therapy induced a moderate effect (+10.5 days median, $P < 0.01$, compared to control nonirradiated mice) (Extended Data Fig. 6b). Strikingly, combination of FLASH RT with GD2 CAR-T cell therapy markedly improved animal survival, with 80% of the mice remaining alive when experiments reached the endpoint on day 60 (Extended Data Fig. 6b). The combination therapy also substantially inhibited tumor growth (Extended Data Fig. 6c).

We determined the effects of FLASH RT on CAR-T cell infiltration and function in vivo. Whole-body bioluminescence imaging showed that FLASH RT but not standard RT robustly improved the homing of

https://doi.org/10.1038/s43018-025-00905-6

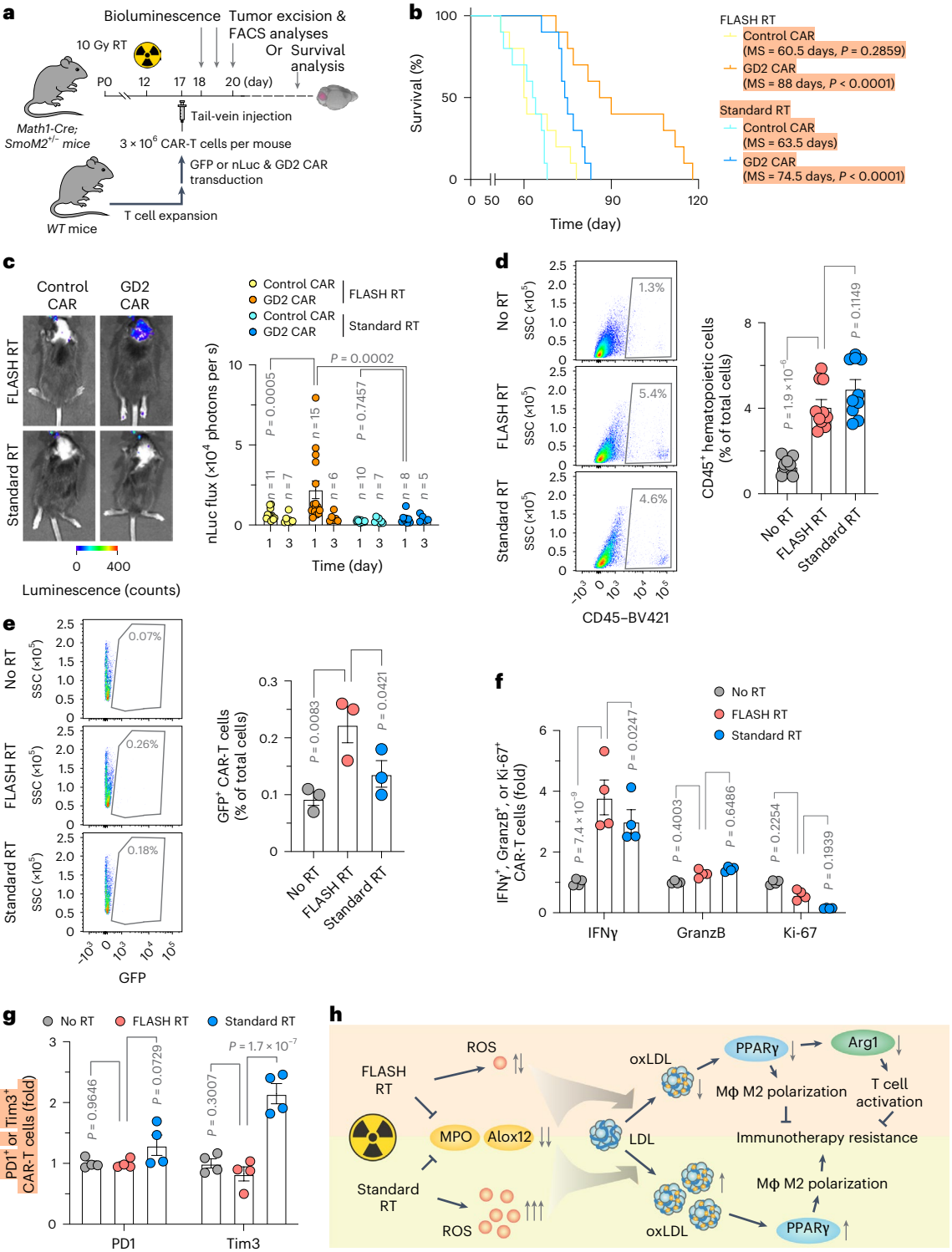

Fig. 6 | FLASH RT overcomes MB resistance to GD2 CAR-T cell immunotherapy. SmoM2 mice were irradiated and treated with control or GD2 CAR-T cells. **a**, Experimental procedures. **b**, Animal survival was monitored ($n = 10$ mice). Statistical analysis by log-rank test. **c**, CAR-T cell infiltration was imaged by bioluminescence. Left, representative images. Right, quantified results on days 1 and 3 after CAR-T cell injection ($n = 5$–15 mice; specific n value of each group listed in the figure; mean ± s.e.m.). Statistical analysis by two-way ANOVA. **d**–**g**, Tumors were excised 3 days after CAR-T cell therapy, followed by flow cytometry analysis. **d**, $CD45^+$ hematopoietic cells. Left, representative cell sortings. Right, quantified results ($n = 10$ mice, mean ± s.e.m.). Statistical analysis by one-way ANOVA. **e**, GFP^+ CAR-T cells. Left, representative cell sortings. Right, quantified results ($n = 3$ mice, mean ± s.e.m.). Statistical analysis by one-way ANOVA. **f**, $IFN\gamma^+$, $GranzB^+$ and $Ki67^+$ GFP^+ CAR-T cells. Quantified results ($n = 4$ mice, mean ± s.e.m.). Statistical analysis by two-way ANOVA. **g**, $PD1^+$ and $Tim3^+$ GFP^+ CAR-T cells. Quantified results ($n = 4$ mice, mean ± s.e.m.). Statistical analysis by two-way ANOVA. **h**, A schematic model. FLASH radiation abrogates expression of oxidases including Mpo and Alox12 and slightly stimulates ROS generation in Mφs, culminating in decreases in oxLDL production and PPARγ activation, which in turn increases T cell activity through reduced arginase 1 (*Arg1*) expression and enhances Mφ M1-like proinflammatory polarization, eventually overcoming tumor resistance to T cell-based cancer immunotherapy. Standard RT also abolishes oxidase expression but robustly enhances ROS production in Mφs, resulting in increases in oxLDL production and PPARγ activation, which drives Mφ M2-like anti-inflammatory polarization and induces tumor resistance to immunotherapy.

these nanoluciferase (nLuc)-expressing CAR-T cells to the MB tumors (Fig. 6c), likely contributing to the survival benefits in the group of mice that received FLASH RT plus GD2 CAR-T combination therapy. Furthermore, our flow cytometry analysis of the MB tumors excised 3 days after CAR-T cell therapy showed that FLASH RT and standard RT stimulated the infiltration of total hematopoietic cells into the tumor at a similar level (Fig. 6d); however, FLASH RT but not standard RT markedly enhanced CAR-T cell infiltration (Fig. 6e). Moreover, compared to standard RT, FLASH RT more robustly stimulated expression of interferon-γ (IFNγ), a major T cell cytotoxic cytokine, and induced less reduction of expression of Ki67, a proliferative marker, in the infiltrated CAR-T cells (Fig. 6f). Furthermore, FLASH RT did not affect expression of programmed cell death protein 1 (PD1) and Tim3, two T cell exhaustion-associated markers, in the infiltrated CAR-T cells (Fig. 6g). In addition, we analyzed the tumors excised 7 days after CAR-T cell therapy (Extended Data Fig. 7a). Similarly, our data showed enhanced CAR-T infiltration by FLASH RT but not by standard RT at that time (Extended Data Fig. 7b). Moreover, FLASH RT rather than standard RT stimulated IFNγ expression in the CAR-T cells (Extended Data Fig. 7c, left). Both FLASH RT and standard RT inhibited PD1 and Tim3 expression in the CAR-T cells (Extended Data Fig. 7c, right), suggesting a time-dependent effect of combination therapy on T cell functions. In a parallel study, we tested a different therapeutic window for the RT and CAR-T cell combination therapy, in which mice were treated with GD2 CAR-T cells 3 days after the irradiation, followed by tumor analysis 6 days later (Extended Data Fig. 7d). Our data showed that FLASH RT but not standard RT consistently stimulated CAR-T cell infiltration (Extended Data Fig. 7e). Neither FLASH RT nor standard RT affected granzyme B (GranzB) or Ki67 expression in the CAR-T cells but FLASH RT stimulated more IFNγ expression in the CAR-T cells than standard RT (Extended Data Fig. 7f). Furthermore, neither FLASH RT nor standard RT affected PD1 expression but standard RT rather than FLASH RT increased Tim3 expression (Extended Data Fig. 7g). Together, these findings suggest that FLASH RT improves CAR-T cell infiltration, stimulates more favorable T cell functions and overcomes tumor resistance to GD2 CAR-T cell immunotherapy.

In summary, our work shows that FLASH radiation stimulates proinflammatory M1-like polarization of tumor Mφs in vitro and in vivo and enhances infiltration of endogenous T cells or infused CAR-T cells into MB tumors. We reveal a redox-mediated and PPARγ-mediated mechanism by which FLASH RT may reprogram Mφs to overcome tumor resistance to T cell-based immunotherapy (Fig. 6h).

Discussion

FLASH RT, albeit initially proposed in the 1960s[38,39], is an innovative treatment approach given recent discoveries showing promise in the treatment of solid tumors because of its potential for reduced toxicity in normal tissues[24–28]. However, its therapeutic effects on tumor immunity, particularly on Mφ functions, remain largely unclear. Here, we report that FLASH RT modulates lipid metabolism to reprogram tumor-associated Mφs toward proinflammatory polarization and reduces Mφ-mediated tumor immunosuppression, empowering CAR-T cell infiltration into the tumors and sensitizing autochthonous MB to CAR-T cell immunotherapy. Because we used a primary mouse model of cancer that coevolves with the immune system, we investigated the impact of FLASH RT in a native tumor immune microenvironment, which is not subject to the influence of tumor cell transplantation that alters the response to the combination of RT and immunotherapy[40]. Consistent with our findings, a recent report showed that FLASH RT increases antitumor Mφs and reduce protumor Mφs in lung cancer[41]. FLASH RT is, therefore, a promising combination partner for cancer immunotherapy, particularly in the context of primary brain tumors, considering its additional benefits of reduced neurocognitive side effects[29,42].

Our work reveals that FLASH and standard RT induces PPARγ inactivation and activation, respectively. A critical and requisite role has been well established for PPARγ in M2 polarization of tumor Mφs[31,43]. PPARγ is a ligand-activated TF that is essential for the regulation of metabolism, inflammation, proliferation and differentiation and can be activated by naturally occurring ligands (for example, polyunsaturated fatty acids) and pharmacologically synthesized agents (for example, rosiglitazone)[44]. Our initial study showed that ROS scavenger TEMPO inhibits PPARγ activity and arginase 1 expression in standard RT-irradiated Mφs, indicating that standard RT-evoked PPARγ activation depends on redox stress. Furthermore, we found that FLASH RT decreases oxLDL production while standard RT increases it, implying that FLASH RT may disrupt oxLDL formation to reduce PPARγ-mediated Mφ immunosuppression. Supporting this hypothesis, 9-HODE and 13-HODE, two major oxidized lipid components of oxLDL, can directly bind and activate PPARγ[45–47]; a structural study validated the interaction of PPARγ with oxidized fatty acids, including 4-HDHA, 5-HEPA and 6-HOTE, leading to greater activation of PPARγ than unoxidized forms[32]. However, as an established marker for cardiovascular disease, the circulating oxLDL, which is favored by polyunsaturated fatty acids rather than monounsaturated fatty acids[33], stimulates proinflammatory responses by binding to its cellular surface receptors, suggesting that oxLDL and PPARγ may have different roles in cancer and cardiovascular diseases.

Fatty acid oxidation can proceed through either lipid oxidases or ROS-mediated direct reaction. Strikingly, our study showed that FLASH RT reduces production of oxLDL, which consists of oxidated cholesterol, fatty acid and protein components, likely acting primarily through downregulation of oxidases including Alox12 and MPO, as FLASH does not robustly stimulate ROS generation in Mφs. Despite inducing similar downregulation of these oxidases, standard RT does not decrease oxLDL production, possibly because of robustly induced ROS. The precise mechanism underlying the oxidase downregulation remains obscure but may be related to an adaptive gene transcription response after RT-induced mitochondrial damage and subsequent lipid metabolism dysfunction. In accordance with our findings showing that FLASH RT does not robustly stimulate ROS production, growing evidence suggests that FLASH RT generates fewer ROS in various cells than standard RT[29,48]. The potential mechanisms may involve different responses in oxygen depletion[29,49–51] or in potential mitochondrial dysfunction induced by FLASH and standard RT. In addition, considering that activated Mφs produce ROS to combat foreign substances, Mφs can generally tolerate a higher level of ROS to maintain redox homeostasis, likely because of the possibility that Mφs may possess a greater reserve capacity for the enzymatic reduction of ROS and can, therefore, remove them more rapidly, potentially contributing to the minimal effects of FLASH RT on intracellular ROS level in Mφs.

T cell-based immunotherapies including checkpoint inhibition and adoptive cell transfer with CAR-modified T cells currently show efficacy in a minority of persons with solid tumors. This is in part because of an immune-hostile microenvironment that limits T cell infiltration into and activation in the tumor. In particular, immunologically cold tumors such as the majority of primary brain tumors are characterized by very few or no infiltrating T cells[4]. Improving T cell recruitment into the tumors is, therefore, critically needed to enhance the success of immunotherapy. Our study shows that FLASH RT enhances GD2 CAR-T cell infiltration into MB tumors, likely because of the reversal of PPARγ-mediated Mφ immunosuppression. In addition, this can be attributed to the potential reduction of TGFβ, a known immunosuppressive cytokine, considering that FLASH RT induces less TGFβ expression in normal tissue[25,27,52,53]. Disialoganglioside GD2 is commonly overexpressed in pediatric and adult solid tumors, such as MB, neuroblastoma and glioma[34,35,54]. Anti-GD2 monoclonal antibodies including naxitamab and dinutuximab represent the standard of care for persons with high-risk neuroblastoma. GD2 CAR-T therapy shows robust efficacy in mouse xenograft models with human MB tumors[54] but exhibits a moderate therapeutic response in glioma and its efficacy is restricted by the immunosuppressive microenvironment[55,56]. Mφs are a major cell population in primary

brain tumors, serving as a key source of tumor immunosuppression and causing resistance to immunotherapy[7–15]. We show that FLASH RT overcomes tumor resistance to GD2 CAR-T cell therapy, likely because of inhibited Mϕ-mediated immunosuppression and reduced arginase 1 release from Mϕs. It is tempting to speculate that FLASH RT may spare tumor vasculature to allow T cell delivery into the tumor given growing evidence that FLASH RT has a less toxic effect on blood vessels in normal tissues than standard RT[25,57,58]; however, the specific effects of FLASH RT on tumor vasculature remain to be investigated.

In sum, our study reveals an ROS-driven and oxidase-driven mechanism that contributes to FLASH RT-induced proinflammatory polarization through oxLDL and PPARγ, providing molecular insight into FLASH RT-modulated tumor immunity. Thus, combined FLASH–CAR-T radioimmunotherapy may offer exciting opportunities for treating pediatric brain tumors and possibly other malignant solid tumors.

Methods

Ethics statement

Research conducted in this manuscript complies with all relevant ethical regulations at the University of Pennsylvania. All experiments with mice were conducted in accordance with protocols (805096 and 806643) approved by the Institutional Animal Care and Use Committee at the University of Pennsylvania. University of Pennsylvania guidelines for the proper and humane use of animals in biomedical research were followed. The protocol for human monocyte and T cell collection was reviewed and approved by the Institutional Review Board of the University of Pennsylvania, with each participant providing written informed consent.

CAR-T cells

Spleen-derived T cells were isolated from C57/B6 mice (2 months old, half male and half female, Jackson laboratory) by mechanical dissociation using a gentleMACS dissociator (Miltenyi Biotech), followed by filtration through a sterile 70-µm strainer (NETA, 410-0002-OEM). T cells were isolated using an EasySep mouse T cell isolation kit (StemCell, 19851). T cells were cultured in Iscove's modified Dulbecco's medium with 10% FBS. T cells were treated with anti-CD3ε and anti-CD28 antibodies (1 µg ml^{-1}; BioLegend, 100302 and 102102) and recombinant IL-2 (100 IU per ml, Peprotech, 212-12) for 2 days. Before retrovirus transduction, non-tissue-treated 6-well or 12-well plates were treated with retronectin (20 µg ml^{-1} in PBS; Takara, T100A) at 4 °C overnight. Retrovirus expressing GFP–nLuc, mouse GD2 CAR or control scFV-free CAR sequence was prepared in Phoenix cells cotransfected with a pCL-Eco helper plasmid using Lipofectamine 2000 (Life Technologies, 11668-019)[37,59]. Cells were immunostained with biotinylated protein L (Life Technologies, 29997) to analyze CAR expression using an FACSCanto II flow cytometer (BD Biosciences). The flow cytometry data were analyzed using FlowJo (version 10.8.1) software. A CAR-T cell-killing assay was performed[60].

Animal model and treatment

Genetically engineered MB was induced in mice[61–64]. In brief, *Math1-Cre*;*SmoM2*$^{fl/fl}$ (Rosa-LSL-Smo$^{W539L/YFP}$) mice were generated by breeding *SmoM2*$^{fl/fl}$ mice with *Math1-Cre* mice, both on a C57/B6 background. The genotype was validated by PCR analysis of genomic DNA using the following primers: Math1-Cre forward, 5′-CCGGCAGAGTTTAC AGAAGC-3′; Math1-Cre reverse, 5′-ATGTTTAGCTGGCCCAAATG-3′; SmoM2$^{WT\ (wild\ type)}$ forward, 5′-CTGGCTTCTGAGGACCG-3′; SmoM2^{WT} reverse, 5′-AGCCTGCCCAGAAGACTCC-3′; SmoM2^{mutant} forward, 5′-TCCCCATCAAGATCCATTTC-3′; SmoM2^{mutant} reverse, 5′-CTGAAC TTGTGGCCGTTTAC-3′. Mice (2 months old, half male and half female, Jackson laboratory) were administrated with CAR-T cells (5×10^6 cells per mouse) through the tail vein. For T cell imaging, mice were infused with mouse T cells coexpressing GD2 CAR or control CAR with tdTomato–nLuc (3×10^6 cells per mouse) through the tail vein. After retro-orbital injection of coelenterazine (10 mg kg^{-1}; Furimazine), mice were imaged. For induction of glioma in mice, 3×10^5 mouse fLuc-expressing GL261 glioma cells (PerkinElmer, 134246) were orthotopically injected into the brains of WT C57BL/6 mice (6–8 weeks old, half male and half female). Survival after injection was monitored for up to 180 and 60 days for MB and glioma, respectively. Mice were injected with luciferin (150 mg kg^{-1}; GoldBio), followed by whole-body bioluminescence analysis using an IVIS 200 Spectrum imaging system to monitor tumor growth. When exhibiting severe glioblastoma symptoms including hemiparesis, dome head or more than 20% body weight loss, tumor-bearing mice were killed. Mice were randomized to receive treatment and the investigators were not blinded. All animals used in this study were housed in the animal facility accredited by the Association for the Assessment and Accreditation of Laboratory Animal Care at the University of Pennsylvania.

Stereotactic RT

A cyclotron-generated 230-MeV proton beam (IBA) was directed horizontally through scattered and collimated system for irradiation[65]. The EBT3 film (Ashland Advanced Materials) was used to check the dose uniformity and alignment. The juvenile mice cerebellum region was aligned with a circular field of 8 mm in diameter and subjected to radiation at the proton beam entrance region. For the dosimetry of such a small field, a Faraday cup was used to capture the proton fluence cross-calibrated with the dose under a large uniform field with an EBT3 film and a reference Advanced Markus ion chamber (PTW Freiburg)[66]. The double-scattering and collimation apparatus was dosimetrically verified with dose rates[65,67]. The dose rate was derived from the measured dose and the irradiation duration captured from an oscilloscope (Tektronix). The proton beam can be delivered at drastically different beam current, resulting in a standard dose rate of 0.7–0.9 Gy s^{-1} or a FLASH ultrahigh dose rate of 97–143 Gy s^{-1}. The cells were also subjected to radiation within the beam's entrance (plateau) region with a circular field of 26-mm diameter using two distinct modalities: FLASH and standard. The FLASH modality exhibited a dose rate spanning approximately 80 to 135 Gy s^{-1}, while the conventional standard modality operated within the range of 0.60 to 0.85 Gy s^{-1}. These variable dose rates were attained by manipulating the cyclotron current, which ranged from 360 nA to 2 nA for FLASH and conventional standard modalities, respectively. Mice were irradiated with the entrance (plateau) region of the beam with a field size of an 8-mm-diameter circular collimator at the hind brains. Cells cultured in the plates were irradiated. The total doses used were 10 Gy for mice and 5 Gy for cells.

Single-cell RNAseq

Treated *Math1-Cre*;*SmoM2*$^{fl/fl}$ mice bearing MB tumors were killed and perfused with PBS containing EDTA. Tumor tissue was excised, followed by digestion with collagenase II (5 mg ml^{-1}; Invitrogen, 17101-015) and DNase (1 mg ml^{-1}; Sigma-Aldrich, D4527). A single-cell suspension was harvested after filtering using a mesh strainer with 70-µm pores (NETA, 410-0002-OEM). Cell samples were pooled from three mouse tumors for each group and were prepared and analyzed according to the manufacturer's V3 library protocol (10x Genomics), followed by single-cell RNAseq analysis at the Center for Applied Genomics of the Children's Hospital of Philadelphia. Reads were aligned using CellRanger (10x Genomics, version 6.1.2) against a mouse reference library (mouse genome assembly GRCm38/mm10). The gene expression matrices that passed default quality control metrics were integrated and analyzed by Seurat R package (version 4.0.6) using sctransform (version 2)[68,69]. The downstream analysis was then conducted using Seurat[68].

Bulk RNAseq analysis

Treated mouse bone marrow-derived Mϕs were lysed using TRIzol (Thermo Fisher Scientific) and RNA was isolated according to the manufacturer's instructions. RNA was purified using an RNeasy Plus mini kit

(QIAGEN). DNA library was prepared with a TruSeq mRNA stranded kit (Illumina). The quality of prepared RNA and library DNA was analyzed with RNA Nano assay chips, RNA Pico assay chips and DNA Nano assay chips using a 2100 Bioanalyzer (Agilent). The library was subject to next-generation sequencing analysis with a NovaSeq at Azenta Life Sciences. The sequences were aligned to the mouse genome assembly GRCm38/mm10 using Kallisto (version 0.46.0). The gene expression was normalized and calculated as counts per million values by R packages tximport (version 1.30.0) and EdgeR (version 3.14.0).

Mouse and human Mϕ isolation and treatment

Mouse bone marrow-derived Mϕs were isolated[31,70]. Freshly isolated femur and tibia bones from C57BL/6 mice (6–8 weeks old, half male and half female) were flushed with RPMI-1640 culture medium (Life Technologies). Cells were harvested and passed through a 40-μm strainer. ACK lysis buffer (Thermo Fisher Scientific) was used to deplete red cells. Bone marrow cells were cultured in RPMI-1640 medium containing 5% FBS (Life Technologies). Cells were treated with 10 ng ml^{-1} mouse colony-stimulating factor 1 (CSF1; PeproTech, 315-02) for 7 days to induce Mϕ differentiation, followed by treatment with 100 ng ml^{-1} LPS (Sigma-Aldrich, LPS25) or 20 ng ml^{-1} IL-4 (BioLegend, 574302) for 2 days with or without pretreatment with 1 mM TEMPO (Targetmol, T5363) or DMTU (Targetmol, T40615). Human PBMC-derived monocytes were isolated from the healthy volunteers, aged 16–64, and provided by the Human Immunology Core of the University of Pennsylvania. The monocytes were treated with human CSF1 (10 ng ml^{-1}; BioLegend, 574806) in RPMI-1640 medium for 5 days to induce differentiation into Mϕs, followed by treatment with LPS (100 ng ml^{-1}; Sigma-Aldrich, LPS25) or human IL-4 (20 ng ml^{-1}; Peprotech, 200-04). The treated Mϕs were also cocultured with human T cells (isolated from healthy volunteers and provided by Human Immunology Core of the University of Pennsylvania). For CFSE staining in T cells, 5×10^7 T cells per ml were incubated with 5 μM CFSE (BioLegend, 423801) for 20 min at 37 °C. The staining was quenched and the treated cells were analyzed.

Flow cytometry

Mouse tumor-derived single-cell suspensions, mouse bone marrow-derived Mϕs and human PBMC-derived Mϕs and were immunostained with fluorescent dye-conjugated antibodies to CD3 (1:100; BioLegend, 100203/100233), CD4 (1:100; BioLegend, 100540), CD8a (1:100; BioLegend, 100706/100708/100733), CD45 (1:100; BioLegend, 103133/103134), F4/80 (1:100; BioLegend, 123107), CD206 (1:100; BioLegend, 141719), CD80 (1:100; BioLegend, 104713, 375403), CD86 (1:100; BioLegend, 105005; 1:100, Miltenyi Biotec, 130-102-604), IFNγ (1:100; BioLegend, 505825), GranzB (1:100; BioLegend, 372211), Ki67 (1:100; Thermo Fisher Scientific, 17-5698-80), LAG3 (1:100; eBioscience, 11-2231-80; BioLegend, 125225/125209), PD1 (1:100; BioLegend, 135223), Tim3 (1:100; BioLegend, 134009), CD11b (1:100; BioLegend, 101206/101212), CD206 (1:100; BioLegend, 321109), NK1.1 (1:100; BioLegend, 156505), TMEM119 (1:100; Thermo Fisher Scientific, 25-6119-80), CD25 (1:100; BioLegend, 101915/302610), GD2 (1:100; BioLegend, 357324) or control IgG[71]. For intracellular staining, cells were treated with TF staining buffer (Thermo Fisher Scientific, 00-5523-00). Cells were analyzed using an FACSCanto II flow cytometer (BD Biosciences) and FlowJo software (version 10.8.1).

Real-time RT–PCR analysis

RNA was extracted from mouse Mϕs using the RNeasy Plus mini kit (QIAGEN, 74136) according to the manufacturer's instructions. Real-time RT–PCR was conducted using the Superscript III first-strand synthesis system (Thermo Fisher Scientific, 12574026) and the powerSYBR Green PCR master mix (Applied Biosystems, 4367659), followed by analysis a QuantStudio 6 Flex system (Applied Biosystems). The primers used were as follows: Arg1 forward, 5′-CTCCAAGCCAAAGTCCTTAGAG-3′, Arg1 reverse, 5′-AGGAGCTGTCATTAGGGACATC-3′, IL-1β forward, 5′-GCAACTGTTCCTGAACTCAACT-3′, IL-1β reverse, 5′-ATCTTTTGGG GTCCGTCAACT-3′, Mpo forward, 5′-AGTTGTGCTGAGCTGTATGGA-3′; MPO reverse, 5′-CGGCTGCTTGAAGTAAAACAGG-3′.

Detection of ROS

Treated mouse bone marrow-derived Mϕs were stained and analyzed for detection of total ROS using a Cellular ROS detection assay kit (Abcam, ab113851) following the manufacturer's instructions. Fluorescence intensity was detected using an FACSCanto II flow cytometer (BD Biosciences).

ELISA

Treated mouse bone marrow-derived Mϕs and human PBMC-derived Mϕs were subjected to ELISA. Total protein concentration was measured using a protein assay kit (Bio-Rad, 5000006). For detecting mouse and human PPARγ activity, cells were analyzed using PPARγ ELISA kits following the manufacturer's instructions (Biorbyt, orb775497 and Elabscience, E-EL-H1361, respectively). For measuring oxLDL level, cells were analyzed using a mouse oxLDL kit (Biorbyt, orb782036) and human oxLDL kit (Elabscience, E-EL-H6021). For analysis of mouse TNF and IL-1β, cell lysis was analyzed using a mouse TNF ELISA Kit (Proteintech, KE10002) and a mouse IL-1β ELISA kit (Proteintech, KE10003). Absorbance at 450 nm was detected with a Synergy H4 Hybrid microplate reader (BioTek). The PPARγ activity and oxLDL level were calculated depending on the standard curve and normalized with total protein concentration.

TF activation array

Mouse BM-derived Mϕs were irradiated at 5 Gy, followed by TF activity analysis with a TF activation profiling array (Signosis, FA-1102). In brief, cells were washed and lysed. The lysates were incubated with TF probe mix in TF-binding buffer. The assembly of TF–DNA complexes was isolated using an isolation column, followed by probe hybridization in a 96-well plate coated with probe sequences at 42 °C overnight. The signal of streptavidin–HRP (horseradish peroxidase) conjugates were measured using a Synergy H4 Hybrid microplate reader (BioTek).

Immunoblot

For cell sample preparation, cells were lysed with an NP-40 lysis buffer with a protease inhibitor cocktail (Roche, 11697498001). Total protein (20 μg) was resolved by 4–20% precast SDS–PAGE (Bio-Rad, 456-1094), followed by transfer. PVDF membranes were blotted with anti-arginase 1 antibody (1:500; Santa Cruz, sc-20150) and anti-glyceraldehyde-3-phosphate dehydrogenase antibody (1:3,000; Cell Signaling, 5174) at 4 °C overnight. Proteins were detected with HRP-conjugated secondary antibodies (Bio-Rad) and the bands were imaged by enhanced chemiluminescence development (GE Healthcare, RPN2232) using a Chemidoc Imager (Bio-Rad).

Immunofluorescence

Mouse tumor sections were subject to deparaffinization and rehydration and incubated with antigen retrieval solution (DAKO, S1699) for 20 min at 95 °C. Tissue sections were blocked with PBS containing 5% horse serum for 1 h and incubated with anti-GD2 antibody (1:200, BioLegend, 357302) at 4 °C overnight. After washing with PBS, sections were stained with Alexa Fluor 488-conjugated IgGs (1:500, Life Technologies) for 1 h at room temperature. Images were acquired using an Axio Imager microscope (Zeiss) equipped with an AxioCam 506 monochrome charge-coupled device camera (Zeiss).

Statistics and reproducibility

All statistical tests were performed using Prism software (GraphPad, version 10.0). All statistical tests were two-sided. An unpaired Student's *t*-test was used to measure differences between the two groups. For multiple-group comparisons, one-way or two-way analysis of variance

(ANOVA) was used to determine statistically significant differences between groups. Kaplan–Meier analysis with a log-rank test was performed for survival analysis. A *P* value lower than 0.05 was considered significant. The exact *P* value is shown in each figure. No statistical methods were used to predetermine sample sizes but we used adequate numbers of samples that would provide statistically significant results on the basis of our previous experience. The exact sample sizes are indicated in the figures or figure legends. To ensure the reproducibility of our results, all experiments were conducted with adequate replicates. All in vivo experiments were randomized to each experimental cohort. The investigators were not blinded to allocation during experiments or outcome assessments. Data distribution was assumed to be normal but this was not formally tested. No data were excluded from the analyses.

Reporting summary

Further information on research design is available in the Nature Portfolio Reporting Summary linked to this article.

Data availability

Single-cell and bulk RNAseq data were deposited to the National Center for Biotechnology Information's Gene Expression Omnibus under accession numbers GSE246970 and GSE246969, respectively. All remaining data are available within the article and the Supplementary Information or available from the authors upon request. Source data are provided with this paper.

References

1. Gajjar, A. J. & Robinson, G. W. Medulloblastoma—translating discoveries from the bench to the bedside. *Nat. Rev. Clin. Oncol.* **11**, 714–722 (2014).
2. Northcott, P. A. et al. Medulloblastoma. *Nat. Rev. Dis. Primers* **5**, 11 (2019).
3. Zhao, J. et al. Immune and genomic correlates of response to anti-PD-1 immunotherapy in glioblastoma. *Nat. Med.* **25**, 462–469 (2019).
4. O'Rourke, D. M. et al. A single dose of peripherally infused EGFRvIII-directed CAR-T cells mediates antigen loss and induces adaptive resistance in patients with recurrent glioblastoma. *Sci. Transl. Med.* **9**, eaaa0984 (2017).
5. Xie, Y. J. et al. Nanobody-based CAR-T cells that target the tumor microenvironment inhibit the growth of solid tumors in immunocompetent mice. *Proc. Natl Acad. Sci. USA* **116**, 7624–7631 (2019).
6. Datta, M., Coussens, L. M., Nishikawa, H., Hodi, F. S. & Jain, R. K. Reprogramming the tumor microenvironment to improve immunotherapy: emerging strategies and combination therapies. *Am. Soc. Clin. Oncol. Educ. Book* **39**, 165–174 (2019).
7. Morantz, R. A., Wood, G. W., Foster, M., Clark, M. & Gollahon, K. Macrophages in experimental and human brain tumors. Part 2: studies of the macrophage content of human brain tumors. *J. Neurosurg.* **50**, 305–311 (1979).
8. Hambardzumyan, D., Gutmann, D. H. & Kettenmann, H. The role of microglia and macrophages in glioma maintenance and progression. *Nat. Neurosci.* **19**, 20–27 (2016).
9. Pollard, J. W. Tumour-educated macrophages promote tumour progression and metastasis. *Nat. Rev. Cancer* **4**, 71–78 (2004).
10. Ruffell, B. & Coussens, L. M. Macrophages and therapeutic resistance in cancer. *Cancer Cell* **27**, 462–472 (2015).
11. Ostuni, R., Kratochvill, F., Murray, P. J. & Natoli, G. Macrophages and cancer: from mechanisms to therapeutic implications. *Trends Immunol.* **36**, 229–239 (2015).
12. Sica, A. & Mantovani, A. Macrophage plasticity and polarization: in vivo veritas. *J. Clin. Invest.* **122**, 787–795 (2012).
13. Murray, P. J. & Wynn, T. A. Protective and pathogenic functions of macrophage subsets. *Nat. Rev. Immunol.* **11**, 723–737 (2011).
14. Stein, M., Keshav, S., Harris, N. & Gordon, S. Interleukin 4 potently enhances murine macrophage mannose receptor activity: a marker of alternative immunologic macrophage activation. *J. Exp. Med.* **176**, 287–292 (1992).
15. Weber, M. S. et al. Type II monocytes modulate T cell-mediated central nervous system autoimmune disease. *Nat. Med.* **13**, 935–943 (2007).
16. Golden, E. B., Marciscano, A. E. & Formenti, S. C. Radiation therapy and the in situ vaccination approach. *Int. J. Radiat. Oncol. Biol. Phys.* **108**, 891–898 (2020).
17. Ibuki, Y. & Goto, R. Contribution of inflammatory cytokine release to activation of resident peritoneal macrophages after in vivo low-dose γ-irradiation. *J. Radiat. Res.* **40**, 253–262 (1999).
18. Hosoi, Y. et al. Induction of interleukin-1β and interleukin-6 mRNA by low doses of ionizing radiation in macrophages. *Int. J. Cancer* **96**, 270–276 (2001).
19. Klug, F. et al. Low-dose irradiation programs macrophage differentiation to an iNOS$^+$/M1 phenotype that orchestrates effective T cell immunotherapy. *Cancer Cell* **24**, 589–602 (2013).
20. O'Brien-Ladner, A., Nelson, M. E., Kimler, B. F. & Wesselius, L. J. Release of interleukin-1 by human alveolar macrophages after in vitro irradiation. *Radiat. Res.* **136**, 37–41 (1993).
21. Russell, J. S. & Brown, J. M. The irradiated tumor microenvironment: role of tumor-associated macrophages in vascular recovery. *Front. Physiol.* **4**, 157 (2013).
22. Shao, J., Welch, W. J., Diprospero, N. A. & Diamond, M. I. Phosphorylation of profilin by ROCK1 regulates polyglutamine aggregation. *Mol. Cell. Biol.* **28**, 5196–5208 (2008).
23. Tsai, C. S. et al. Macrophages from irradiated tumors express higher levels of iNOS, arginase-I and COX-2, and promote tumor growth. *Int. J. Radiat. Oncol. Biol. Phys.* **68**, 499–507 (2007).
24. Vozenin, M. C., Hendry, J. H. & Limoli, C. L. Biological benefits of Ultra-high Dose Rate FLASH radiotherapy: sleeping beauty awoken. *Clin. Oncol. (R. Coll. Radiol.)* **31**, 407–415 (2019).
25. Favaudon, V. et al. Ultrahigh dose-rate FLASH irradiation increases the differential response between normal and tumor tissue in mice. *Sci. Transl. Med.* **6**, 245ra293 (2014).
26. de Kruijff, R. M. FLASH radiotherapy: ultra-high dose rates to spare healthy tissue. *Int. J. Radiat. Biol.* **96**, 419–423 (2020).
27. Velalopoulou, A. et al. FLASH proton radiotherapy spares normal epithelial and mesenchymal tissues while preserving sarcoma response. *Cancer Res.* **81**, 4808–4821 (2021).
28. Mascia, A. E. et al. Proton FLASH radiotherapy for the treatment of symptomatic bone metastases: the FAST-01 nonrandomized trial. *JAMA Oncol.* **9**, 62–69 (2023).
29. Montay-Gruel, P. et al. Long-term neurocognitive benefits of FLASH radiotherapy driven by reduced reactive oxygen species. *Proc. Natl Acad. Sci. USA* **116**, 10943–10951 (2019).
30. Menjivar, R. E. et al. Arginase 1 is a key driver of immune suppression in pancreatic cancer. *eLife* **12**, e80721 (2023).
31. Wang, Q. et al. Vascular niche IL-6 induces alternative macrophage activation in glioblastoma through HIF-2α. *Nat. Commun.* **9**, 559 (2018).
32. Itoh, T. et al. Structural basis for the activation of PPARγ by oxidized fatty acids. *Nat. Struct. Mol. Biol.* **15**, 924–931 (2008).
33. Reaven, P. et al. Effects of oleate-rich and linoleate-rich diets on the susceptibility of low density lipoprotein to oxidative modification in mildly hypercholesterolemic subjects. *J. Clin. Invest.* **91**, 668–676 (1993).
34. Paret, C. et al. GD2 expression in medulloblastoma and neuroblastoma for personalized immunotherapy: a matter of subtype. *Cancers (Basel)* **14**, 6051 (2022).
35. Del Bufalo, F. et al. GD2-CART01 for relapsed or refractory high-risk neuroblastoma. *N. Engl. J. Med.* **388**, 1284–1295 (2023).

36. Sampson, J. H. et al. EGFRvIII mCAR-modified T-cell therapy cures mice with established intracerebral glioma and generates host immunity against tumor-antigen loss. *Clin. Cancer Res.* **20**, 972–984 (2014).
37. Ma, W. et al. Targeting PAK4 to reprogram vascular microenvironment and improve CAR-T immunotherapy for glioblastoma. *Nat. Cancer* **2**, 83–97 (2021).
38. Hornsey, S. & Alper, T. Unexpected dose-rate effect in the killing of mice by radiation. *Nature* **210**, 212–213 (1966).
39. Town, C. D. Effect of high dose rates on survival of mammalian cells. *Nature* **215**, 847–848 (1967).
40. Wisdom, A. J. et al. Single cell analysis reveals distinct immune landscapes in transplant and primary sarcomas that determine response or resistance to immunotherapy. *Nat. Commun.* **11**, 6410 (2020).
41. Shukla, S. et al. Ultra-high dose-rate proton FLASH improves tumor control. *Radiother. Oncol.* **186**, 109741 (2023).
42. Montay-Gruel, P. et al. Hypofractionated FLASH-RT as an effective treatment against glioblastoma that reduces neurocognitive side effects in mice. *Clin. Cancer Res.* **27**, 775–784 (2021).
43. Ricote, M., Huang, J. T., Welch, J. S. & Glass, C. K. The peroxisome proliferator-activated receptor (PPARγ) as a regulator of monocyte/macrophage function. *J. Leukoc. Biol.* **66**, 733–739 (1999).
44. Peters, J. M., Shah, Y. M. & Gonzalez, F. J. The role of peroxisome proliferator-activated receptors in carcinogenesis and chemoprevention. *Nat. Rev. Cancer* **12**, 181–195 (2012).
45. Nagy, L., Tontonoz, P., Alvarez, J. G., Chen, H. & Evans, R. M. Oxidized LDL regulates macrophage gene expression through ligand activation of PPARγ. *Cell* **93**, 229–240 (1998).
46. Marx, N., Bourcier, T., Sukhova, G. K., Libby, P. & Plutzky, J. PPARγ activation in human endothelial cells increases plasminogen activator inhibitor type-1 expression: PPARγ as a potential mediator in vascular disease. *Arterioscler. Thromb. Vasc. Biol.* **19**, 546–551 (1999).
47. Schild, R. L. et al. The activity of PPARγ in primary human trophoblasts is enhanced by oxidized lipids. *J. Clin. Endocrinol. Metab.* **87**, 1105–1110 (2002).
48. Spitz, D. R. et al. An integrated physico-chemical approach for explaining the differential impact of FLASH versus conventional dose rate irradiation on cancer and normal tissue responses. *Radiother. Oncol.* **139**, 23–27 (2019).
49. Epp, E. R., Weiss, H., Djordjevic, B. & Santomasso, A. The radiosensitivity of cultured mammalian cells exposed to single high intensity pulses of electrons in various concentrations of oxygen. *Radiat. Res.* **52**, 324–332 (1972).
50. Ling, C. C., Michaels, H. B., Epp, E. R. & Peterson, E. C. Oxygen diffusion into mammalian cells following ultrahigh dose rate irradiation and lifetime estimates of oxygen-sensitive species. *Radiat. Res.* **76**, 522–532 (1978).
51. Adrian, G. et al. The FLASH effect depends on oxygen concentration. *Br. J. Radiol.* **93**, 20190702 (2020).
52. Buonanno, M., Grilj, V. & Brenner, D. J. Biological effects in normal cells exposed to FLASH dose rate protons. *Radiother. Oncol.* **139**, 51–55 (2019).
53. Fouillade, C. et al. FLASH irradiation spares lung progenitor cells and limits the incidence of radio-induced senescence. *Clin. Cancer Res.* **26**, 1497–1506 (2020).
54. Ciccone, R. et al. GD2-targeting CAR-T-cell therapy for patients with $GD2^+$ medulloblastoma. *Clin. Cancer Res.* **30**, 2545–2557 (2024).
55. Majzner, R. G. et al. GD2-CAR T cell therapy for H3K27M-mutated diffuse midline gliomas. *Nature* **603**, 934–941 (2022).
56. Thomas, B. C. et al. CAR-T cell therapies for diffuse midline glioma. *Trends Cancer* **9**, 791–804 (2023).
57. Kim, Y. E. et al. Effects of ultra-high doserate FLASH irradiation on the tumor microenvironment in Lewis lung carcinoma: role of myosin light chain. *Int. J. Radiat. Oncol. Biol. Phys.* **109**, 1440–1453 (2021).
58. Allen, B. D. et al. Elucidating the neurological mechanism of the FLASH effect in juvenile mice exposed to hypofractionated radiotherapy. *Neuro Oncol.* **25**, 927–939 (2023).
59. Zhang, D. et al. PHGDH-mediated endothelial metabolism drives glioblastoma resistance to chimeric antigen receptor T cell immunotherapy. *Cell Metab.* **35**, 517–534 (2023).
60. Zhang, D. et al. Protocol to generate traceable CAR-T cells for syngeneic mouse cancer models. *STAR Protoc.* **5**, 102898 (2024).
61. Liu, Y. et al. Somatic cell type specific gene transfer reveals a tumor-promoting function for p21(Waf1/Cip1). *EMBO J.* **26**, 4683–4693 (2007).
62. Ciznadija, D., Liu, Y., Pyonteck, S. M., Holland, E. C. & Koff, A. Cyclin D1 and cdk4 mediate development of neurologically destructive oligodendroglioma. *Cancer Res.* **71**, 6174–6183 (2011).
63. Fan, Y. et al. Profilin-1 phosphorylation directs angiocrine expression and glioblastoma progression through HIF-1α accumulation. *Nat. Cell Biol.* **16**, 445–456 (2014).
64. Huang, M. et al. c-Met-mediated endothelial plasticity drives aberrant vascularization and chemoresistance in glioblastoma. *J. Clin. Invest.* **126**, 1801–1814 (2016).
65. Diffenderfer, E. S. et al. Design, implementation, and in vivo validation of a novel proton FLASH radiation therapy system. *Int. J. Radiat. Oncol. Biol. Phys.* **106**, 440–448 (2020).
66. International Atomic Energy Agency. *Absorbed Dose Determination in External Beam Radiotherapy: An International Code of Practice for Dosimetry Based on Standards of Absorbed Dose to Water*. Technical Reports Series no. 398 (IAEA, 2001).
67. Zou, W. et al. Framework for quality assurance of ultrahigh dose rate clinical trials investigating FLASH effects and current technology gaps. *Int. J. Radiat. Oncol. Biol. Phys.* **116**, 1202–1217 (2023).
68. Hao, Y. et al. Integrated analysis of multimodal single-cell data. *Cell* **184**, 3573–3587 (2021).
69. Hafemeister, C. & Satija, R. Normalization and variance stabilization of single-cell RNA-seq data using regularized negative binomial regression. *Genome Biol.* **20**, 296 (2019).
70. Yang, F. et al. Synergistic immunotherapy of glioblastoma by dual targeting of IL-6 and CD40. *Nat. Commun.* **12**, 3424 (2021).
71. Yang, F. et al. Small-molecule toosendanin reverses macrophage-mediated immunosuppression to overcome glioblastoma resistance to immunotherapy. *Sci. Transl. Med.* **15**, eabq3558 (2023).

Acknowledgements

We are grateful to J. Billings for help with single-cell RNAseq analysis. This work was supported in part by the University of Pennsylvania Abramson Cancer Center Radiation Oncology Translational Center for Excellence (to Y.F.), National Institutes of Health grants R01NS094533 (to Y.F.), R01NS106108 (to Y.F.), R01CA241501 (to J.F.D. and Y.F.), R01HL106108 (to Y.F. and Y.G.), R35CA197616 (to D.G.K), P01CA257904 (to A.J.M., C.K. and D.G.K.) and K08CA256045 (to Z.J.R.) and developmental funds from P30CA014236 (to Z.J.R.) and P50CA190991 Duke SPORE in Brain Cancer (to Z.J.R. and D.G.K.), a Yosemite Award from the American Cancer Society (to Y.F.), a Mark Foundation grant (to A.J.M.), a Pediatric Brain Tumor Foundation grant (to Z.J.R.), a St. Baldrick's Foundation grant (to Z.J.R.), a Chadtough Defeat DIPG grant (to Z.J.R.) and an Alex's Lemonade Stand Foundation grant (to Z.J.R.).

Author contributions

H.N. performed the experiments, analyzed the results and produced the figures. Z.J.R. designed the experiments. W.Z. and S.A.O.M.

conducted the radiation dosimetry and delivery. M.N.A. and R.M. helped with the T cell assays. R.P. and M.H. contributed to the initial in vivo RT experiments. D.Z. and L.Z. contributed to the bioinformatic analysis. H.Z., R.Z. and G.N. helped with the experimental assays. J.B.F. contributed to the GD2 CAR-T treatment. E.S.D., M.M.K., A.M., J.F.D., J.M. and C.K. contributed to the FLASH physics and RT. D.G.K., Y.G. and Y.F. contributed to the experimental design and data interpretation. D.G.K., Y.G. and Y.F. supervised the project. Y.F. conceptualized the ideas and wrote the manuscript. All authors commented on the manuscript.

Competing interests

D.G.K. is a cofounder of and stockholder in XRAD Therapeutics, which is developing radiosensitizers. D.G.K. is a member of the scientific advisory board and owns stock in Lumicell, a company commercializing intraoperative imaging technology. None of these affiliations represent a conflict of interest with respect to the work of this manuscript. D.G.K. is a coinventor on a patent for a handheld imaging device and is a coinventor on a patent for radiosensitizers. None of these patents are relevant to this manuscript. XRAD Therapeutics, Merck, Bristol Myers Squibb and Varian Medical Systems have provided research support to D.G.K. but this did not support the research described in this manuscript. Z.J.R. is listed as an inventor for intellectual property related to genetic testing for brain tumors that is managed by Duke Office of Licensing and Ventures, which is not relevant to this manuscript. The other authors declase no competing interests.

Additional information

Extended data is available for this paper at https://doi.org/10.1038/s43018-025-00905-6.

Supplementary information The online version contains supplementary material available at https://doi.org/10.1038/s43018-025-00905-6.

Correspondence and requests for materials should be addressed to David G. Kirsch, Yanqing Gong or Yi Fan.

Peer review information *Nature Cancer* thanks Niels Bovenschen, Aaron Diaz, Ping-Chih Ho and the other, anonymous, reviewer(s) for their contribution to the peer review of this work.

Reprints and permissions information is available at www.nature.com/reprints.

Publisher's note Springer Nature remains neutral with regard to jurisdictional claims in published maps and institutional affiliations.

Springer Nature or its licensor (e.g. a society or other partner) holds exclusive rights to this article under a publishing agreement with the author(s) or other rightsholder(s); author self-archiving of the accepted manuscript version of this article is solely governed by the terms of such publishing agreement and applicable law.

© The Author(s), under exclusive licence to Springer Nature America, Inc. 2025

Haiwei Ni[1,10], Zachary J. Reitman[2,10], Wei Zou[1], Md Naushad Akhtar[1], Ritama Paul[1], Menggui Huang[1], Duo Zhang[1], Hao Zheng[1], Ruitao Zhang[1], Ruiying Ma[1], Gina Ngo[1], Lin Zhang[3], Eric S. Diffenderfer[1], S. Azar Oliaei Motlagh[1], Michele M. Kim[1], Andy J. Minn[1,4], Jay F. Dorsey[1], Jessica B. Foster[5], James Metz[1], Constantinos Koumenis[1,4], David G. Kirsch[2,6,7,8] ✉, Yanqing Gong[9] ✉ & Yi Fan[1,4] ✉

[1]Department of Radiation Oncology, University of Pennsylvania, Philadelphia, PA, USA. [2]Department of Radiation Oncology, Duke University Medical Center, Durham, NC, USA. [3]Department of Obstetrics and Gynecology, University of Pennsylvania, Philadelphia, PA, USA. [4]Mark Foundation Center for Immunotherapy, Immune Signaling, and Radiation, University of Pennsylvania, Philadelphia, PA, USA. [5]Division of Oncology, Children's Hospital of Philadelphia, Philadelphia, PA, USA. [6]Radiation Medicine Program, Princess Margaret Cancer Centre, Toronto, Ontario, Canada. [7]Department of Radiation Oncology, University of Toronto, Toronto, Ontario, Canada. [8]Department of Medical Biophysics, University of Toronto, Toronto, Ontario, Canada. [9]Department of Medicine, University of Pennsylvania, Philadelphia, PA, USA. [10]These authors contributed equally: Haiwei Ni, Zachary J. Reitman. ✉e-mail: david.kirsch@uhn.ca; gongy@pennmedicine.upenn.edu; fanyi@upenn.edu

https://doi.org/10.1038/s43018-025-00905-6

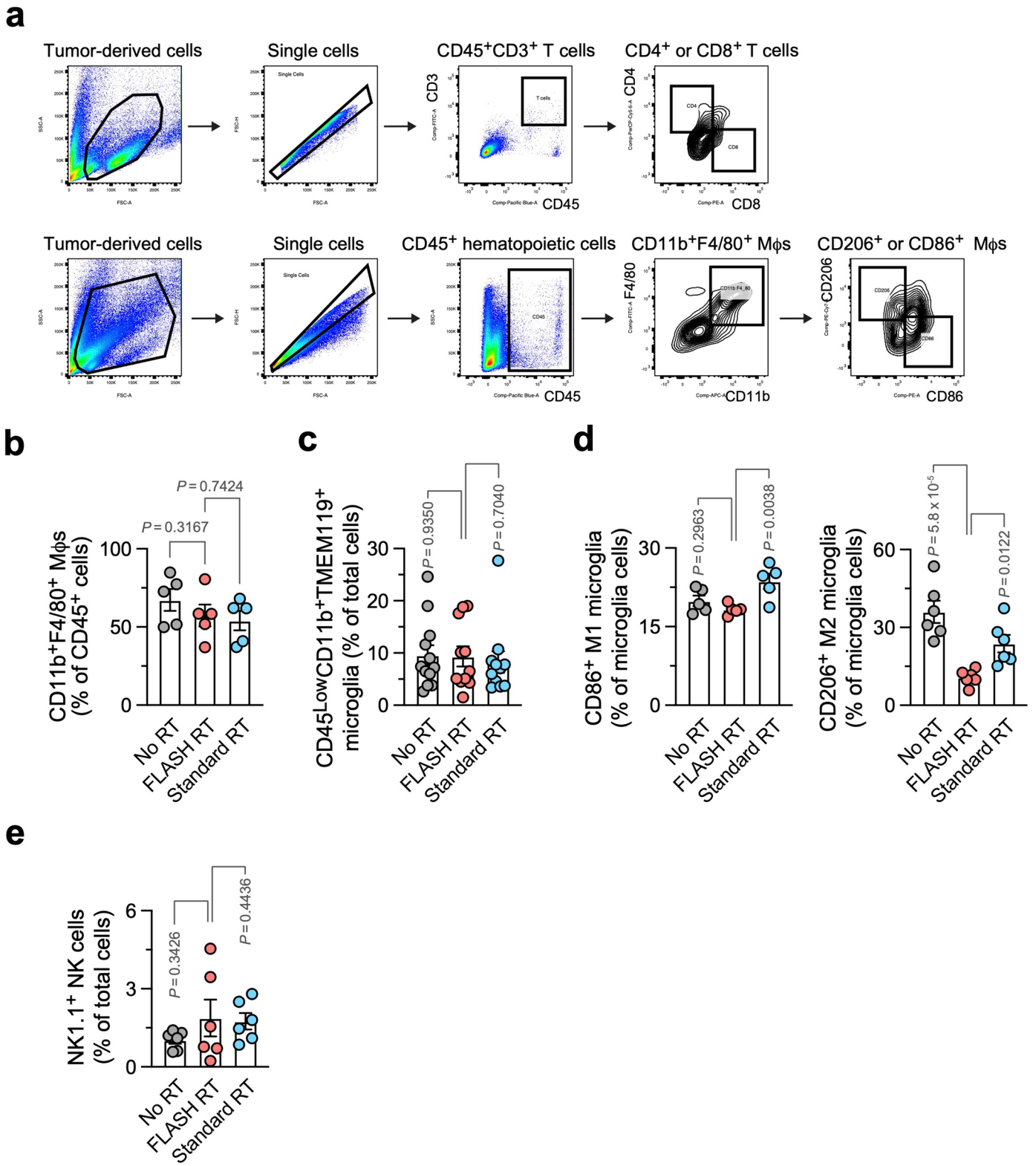

Extended Data Fig. 1 | Effects of RT on tumor-associated Mfs, microglia, and NK cells. Medulloblastoma was genetically engineered in SmoM2 mice, followed by irradiation with FLASH or standard proton beam. Tumors were excised and subjected to flow cytometry analysis. **a**, Gating strategies for analysis of T cells and Mϕs, corresponding to Fig. 1i–o. **b**-**e**, Analysis for **b**, $CD11b^+F4/80^+$ total Mϕs (n = 5 mice), **c**, $CD45^{Low}CD11b^+TMEM119^+$ total microglia (n = 12 mice for no RT group, and n = 11 mice for FLASH and standard RT groups), **d**, $CD86^+$ M1-like (n = 5 mice) and $CD206^+$ M2-like microglia (n = 6 mice), and **e**, $NK1.1^+$ NK cells (n = 6 mice). Statistical analysis by one-way ANOVA (mean ± SEM).

https://doi.org/10.1038/s43018-025-00905-6

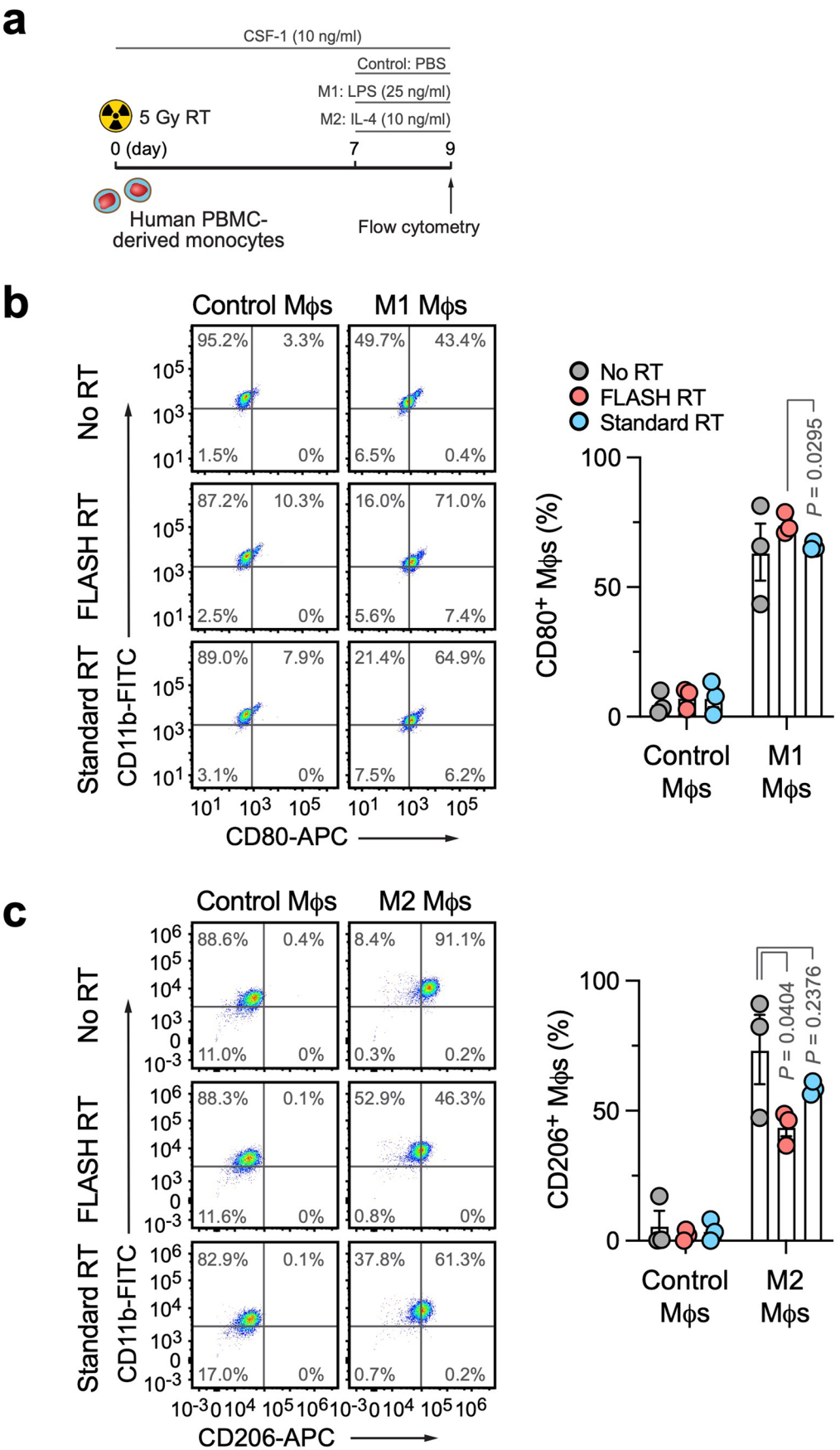

Extended Data Fig. 2 | Effects of RT on human Mf polarization in vitro. Human PBMC-derived Mϕs were irradiated with FLASH or standard proton beam, followed by treatment with LPS or IL-4. **a**, Experimental procedure. **b,c**, After treatment with b, LPS or **c**, IL-4, cells were analyzed by flow cytometry. Left, representative cell sortings. Right, quantified results (n = 3 human participants, mean ± SEM). **b**, Statistical analysis by two-tailed Student's t test. **c**, Statistical analysis by one-way ANOVA.

https://doi.org/10.1038/s43018-025-00905-6

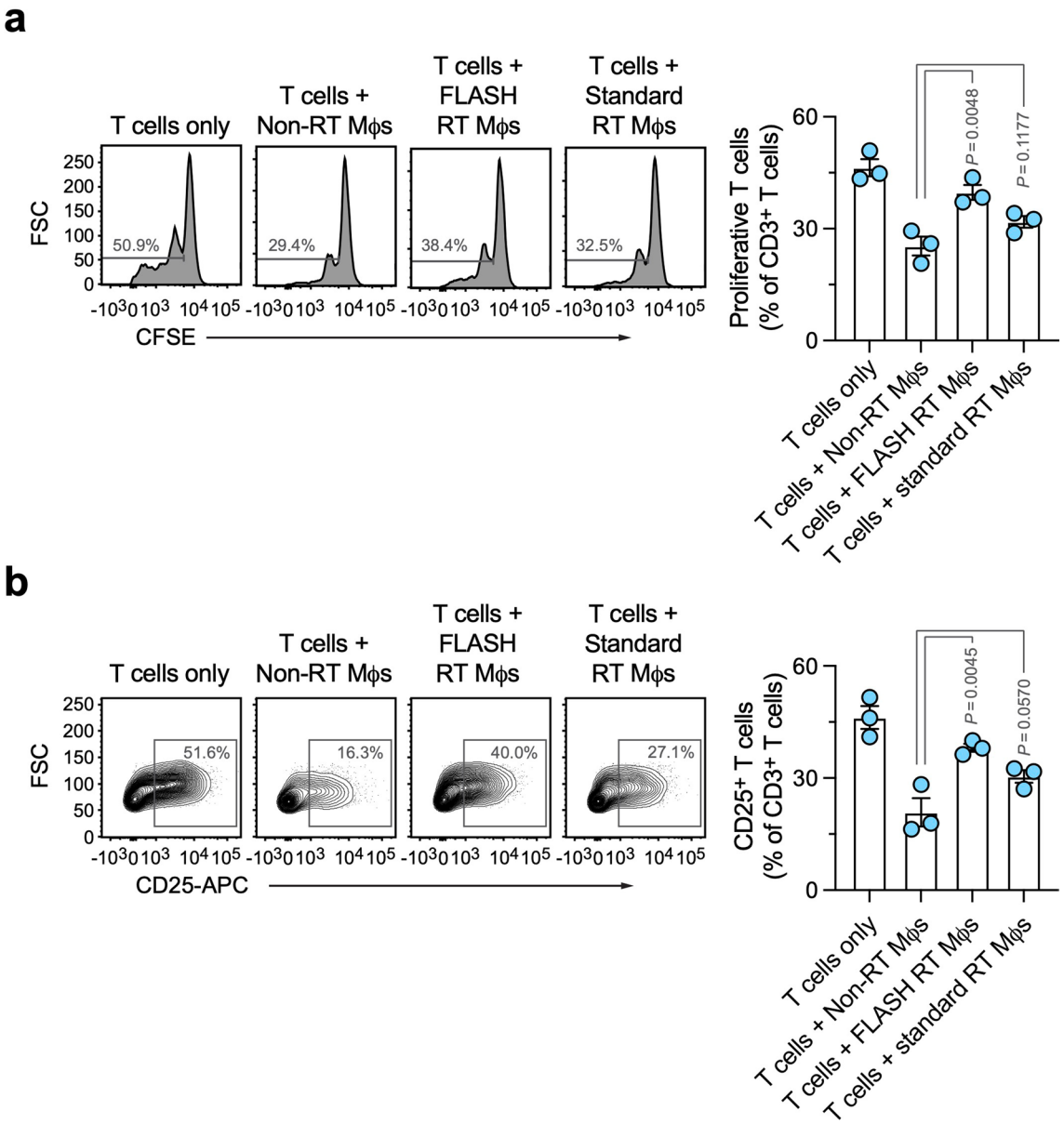

Extended Data Fig. 3 | Effects of irradiated Mfs on T cell functions in vitro. Human PBMC-derived Mϕs cells were irradiated by FLASH or standard proton beam and treated with IL-4 for 2 days. Human PBMC-derived $CD3^+$ T cells were stimulated with CD3/CD28 beads for 3 days, and loaded with CFSE. Treated Mϕs and T cells were incubated for 2 days, followed by flow cytometry analysis. **a**, CFSE was analyzed in $CD3^+$ T cells. Left, representative cell sortings. Right, quantified results (n = 3 human participants, mean ± SEM). Statistical analysis by one-way ANOVA. **b**, CD25 expression was analyzed in $CD3^+$ T cells. Left, representative cell sortings. Right, quantified results (n = 3 human participants, mean ± SEM). Statistical analysis by one-way ANOVA.

https://doi.org/10.1038/s43018-025-00905-6

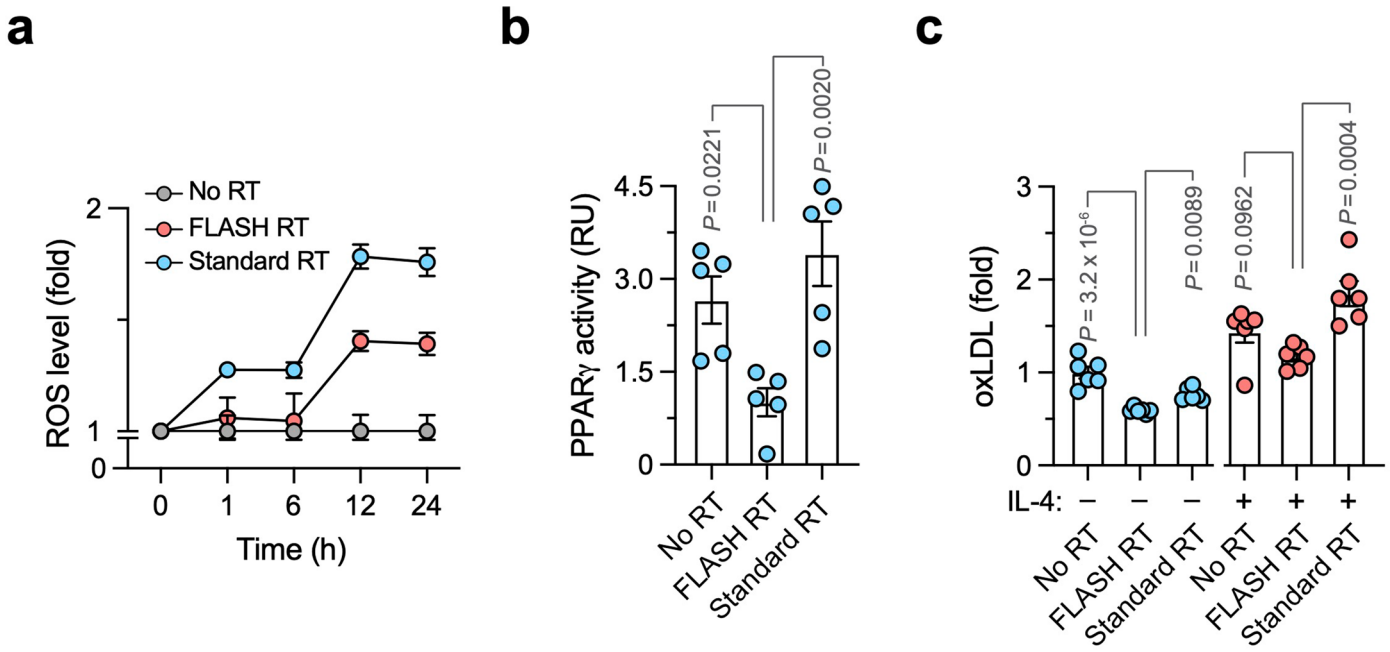

Extended Data Fig. 4 | Effects of RT on ROS generation, PPARg activity and oxLDL production in human Mfs. Human PBMC-derived Mϕs were irradiated with FLASH or standard proton beam. **a**, Total ROS were analyzed at different time post-irradiation (mean ± SEM, n = 3 human participants). **b**, PPARγ activity was measured 24 h after irradiation (mean ± SEM, n = 5 human participants). Statistical analysis by one-way ANOVA. **c**, Human PBMC-derived Mϕs were irradiated with FLASH or standard proton beam, followed by treatment with or without IL-4. Cell lystes were subjected to oxLDL analysis (mean ± SEM, n = 6 human participants). Statistical analysis by one-way ANOVA.

https://doi.org/10.1038/s43018-025-00905-6

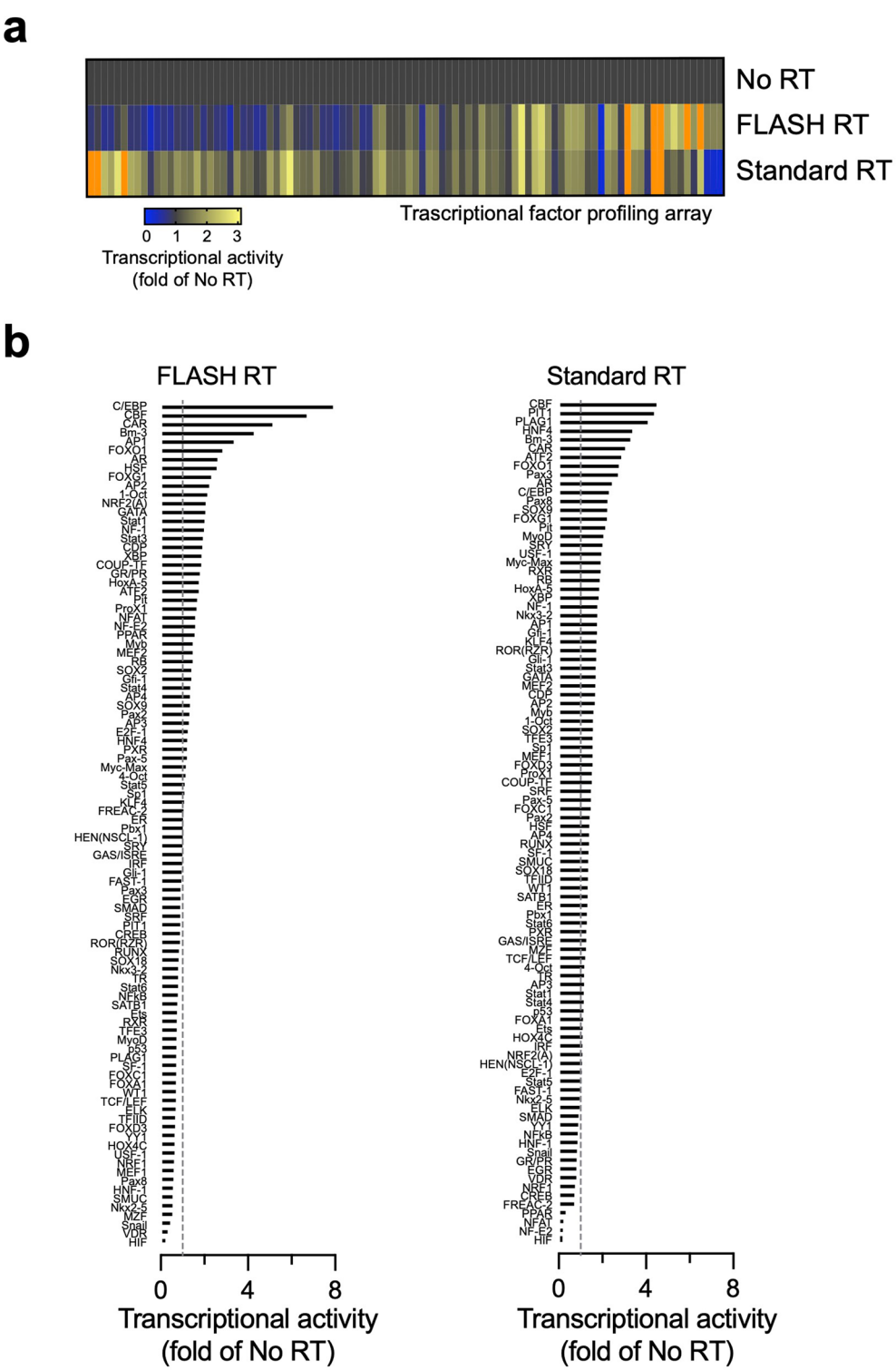

Extended Data Fig. 5 | Effects of RT on trancriptional factor activity in vitro. Mouse BM-derived Mϕs (pooled from 3 mouse samples for each group) were irradiated with FLASH or standard proton beam, and subjected to analysis with a transcriptional factor profiling assay. The activity of 96 transcriptional factors was expressed as the fold of no RT group. **a**, Heatmap. **b**, Ranked activity.

https://doi.org/10.1038/s43018-025-00905-6

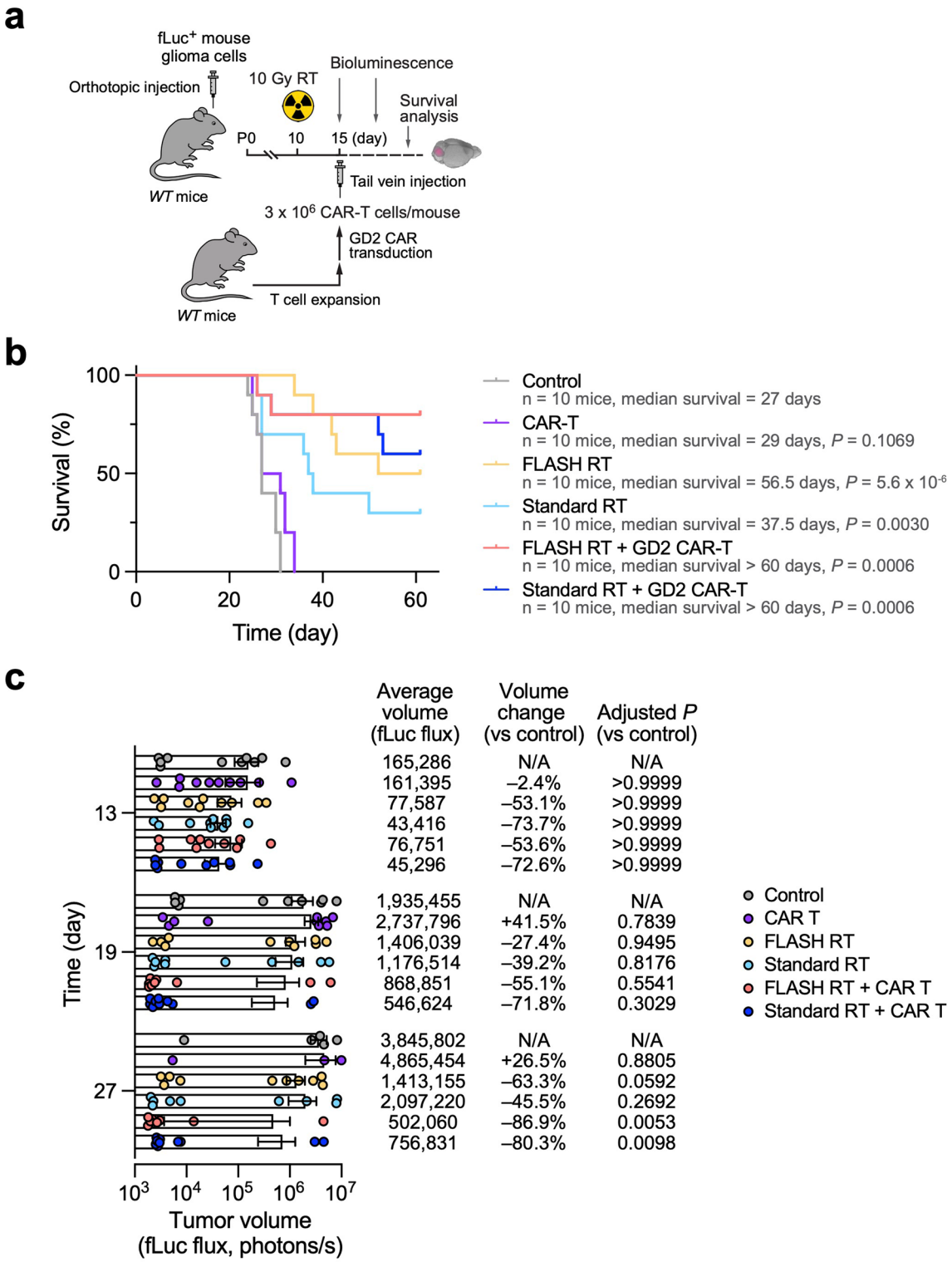

Extended Data Fig. 6 | Combination of RT with CAR T cell therapy in a syngeneic mouse glioma model. Glioma was induced in mice by orthotopic transplantation with GL261 mouse glioma cells, followed by FLASH or standard RT and GD2 CAR-T cell therapy. **a**, Experimental procedures. **b**, Animal survival was monitored for 60 days (n = 10 mice). Statistical analysis by a two-tailed Log-rank Mantel-Cox test. **c**, Tumor volume was measured by bioluminescence imaging (n = 10 mice, mean ± SEM). Note: after standard RT plus CAR T cell treatment, one mouse developed neurological symptoms at late day 26 and was imaged at day 27. Statistical analysis by two-way ANOVA.

https://doi.org/10.1038/s43018-025-00905-6

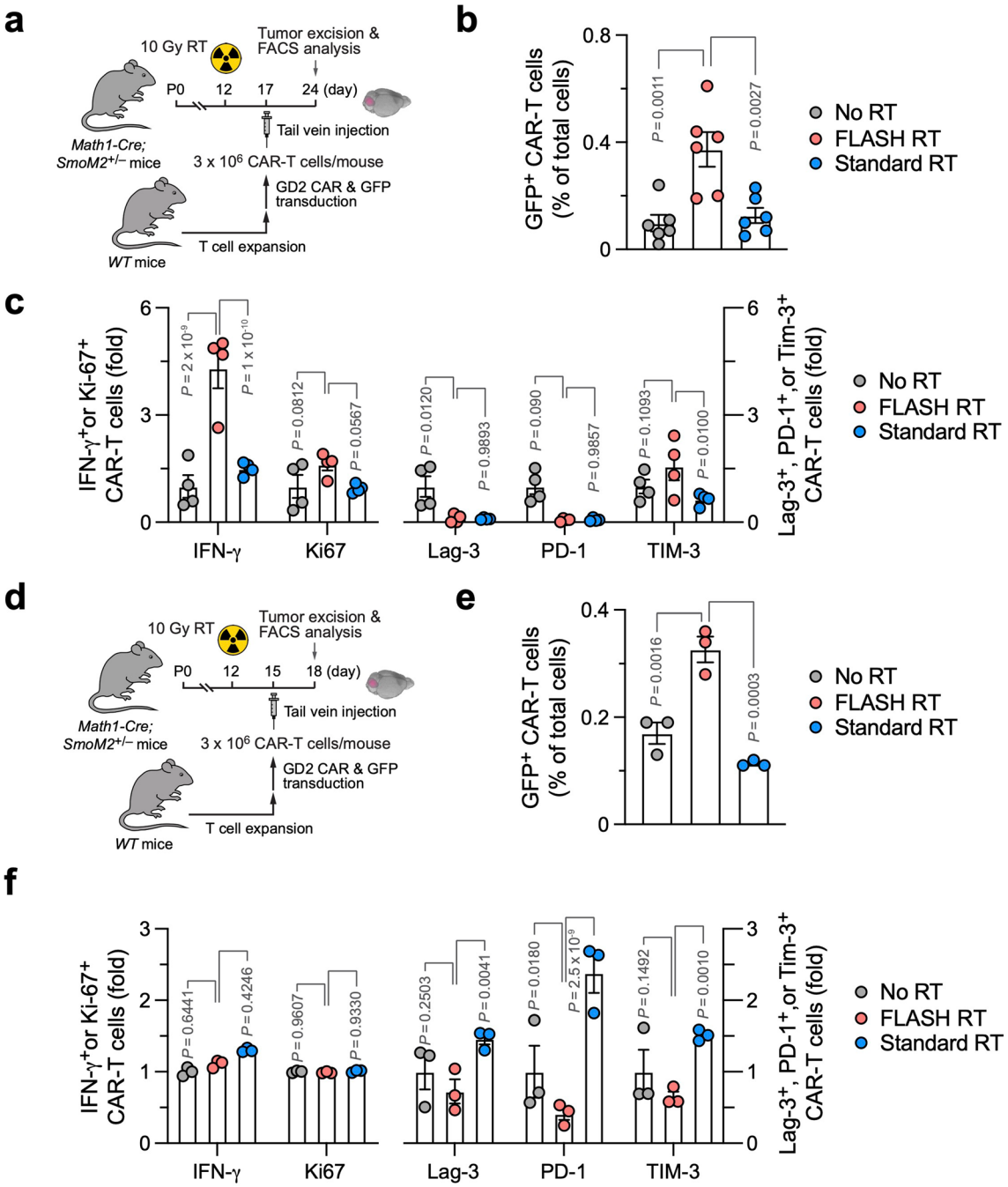

Extended Data Fig. 7 | Effects of RT on CAR T infiltration and activity in vivo. **a-c**, 5 days after irradiation, SmoM2 mice were treated with GD2 CAR-T cells. **a**, Experimental procedures. **b,c**, Tumors were excised 7 days after CAR-T cell therapy, followed by flow cytometry analysis. (**b**, Analysis of GFP$^+$ CAR-T cells (n = 6 mice, mean ± SEM). Statistical analysis by one-way ANOVA. **c**, Analysis of IFN-g$^+$, Ki-67$^+$, Lag-3$^+$, PD-1$^+$ and Tim-3$^+$ GFP$^+$ CAR T cells (n = 4 mice, mean ± SEM). Statistical analysis by two-way ANOVA. **d-e**, 3 days after irradiation, SmoM2 mice were treated with GD2 CAR-T cells. **d**, Experimental procedures. **e,f**, Tumors were excised 3 days after CAR-T cell therapy, followed by flow cytometry analysis. **e**, Analysis of GFP$^+$ CAR T cells (n = 3 mice, mean ± SEM). Statistical analysis by one-way ANOVA. **f**, Analysis of IFN-g$^+$, Ki-67$^+$, Lag-3$^+$, PD-1$^+$ and Tim-3$^+$ GFP$^+$ CAR T cells (n = 3 mice, mean ± SEM). Statistical analysis by two-way ANOVA.

nature portfolio

Corresponding author(s): David Kirsch, Yanqing Gong, Yi Fan

Last updated by author(s): 12/22/2024

Reporting Summary

Nature Portfolio wishes to improve the reproducibility of the work that we publish. This form provides structure for consistency and transparency in reporting. For further information on Nature Portfolio policies, see our Editorial Policies and the Editorial Policy Checklist.

Statistics

For all statistical analyses, confirm that the following items are present in the figure legend, table legend, main text, or Methods section.

n/a	Confirmed
☐	☒ The exact sample size (*n*) for each experimental group/condition, given as a discrete number and unit of measurement
☐	☒ A statement on whether measurements were taken from distinct samples or whether the same sample was measured repeatedly
☐	☒ The statistical test(s) used AND whether they are one- or two-sided *Only common tests should be described solely by name; describe more complex techniques in the Methods section.*
☒	☐ A description of all covariates tested
☐	☒ A description of any assumptions or corrections, such as tests of normality and adjustment for multiple comparisons
☐	☒ A full description of the statistical parameters including central tendency (e.g. means) or other basic estimates (e.g. regression coefficient) AND variation (e.g. standard deviation) or associated estimates of uncertainty (e.g. confidence intervals)
☐	☒ For null hypothesis testing, the test statistic (e.g. *F*, *t*, *r*) with confidence intervals, effect sizes, degrees of freedom and *P* value noted *Give P values as exact values whenever suitable.*
☒	☐ For Bayesian analysis, information on the choice of priors and Markov chain Monte Carlo settings
☒	☐ For hierarchical and complex designs, identification of the appropriate level for tests and full reporting of outcomes
☒	☐ Estimates of effect sizes (e.g. Cohen's *d*, Pearson's *r*), indicating how they were calculated

Our web collection on statistics for biologists contains articles on many of the points above.

Software and code

Policy information about availability of computer code

Data collection	Illumina sequencer NovaSeq for RNAseq data.
Data analysis	FlowJo v10.8.1 for flow cytometry data. Graphpad Prism v10.0 for statistical analysis. CellRanger (10x Genomics) v6.1.2 for read alignment. Seurat R package v4.0.6 for single-cell RNAseq data integration and analysis. Kallisto v0.46.0 for gene alignment in bulk RNAsee analysis. tximport v1.30.0 and EdgeR v3.14.0 R package for bulk RNAseq data analysis.

For manuscripts utilizing custom algorithms or software that are central to the research but not yet described in published literature, software must be made available to editors and reviewers. We strongly encourage code deposition in a community repository (e.g. GitHub). See the Nature Portfolio guidelines for submitting code & software for further information.

Data

Policy information about availability of data

All manuscripts must include a data availability statement. This statement should provide the following information, where applicable:

- Accession codes, unique identifiers, or web links for publicly available datasets
- A description of any restrictions on data availability
- For clinical datasets or third party data, please ensure that the statement adheres to our policy

Data Availability Statement
Single-cell and bulk RNA-seq data have been deposited in NCBI's Gene Expression Omnibus with accession GSE246970 [https://www.ncbi.nlm.nih.gov/geo/query/acc.cgi?acc=GSE246970] and GSE246969 [https://www.ncbi.nlm.nih.gov/geo/query/acc.cgi?acc=GSE246969], respectively.
All remaining data are available within the Article and its Supplementary Files, or available from the authors upon request. Source data are provided with this paper.

Research involving human participants, their data, or biological material

Policy information about studies with human participants or human data. See also policy information about sex, gender (identity/presentation), and sexual orientation and race, ethnicity and racism.

Reporting on sex and gender	Healthy volunteers with all sexes and genders participated this studies.
Reporting on race, ethnicity, or other socially relevant groupings	Healthy volunteers participated this studies, regardless of their race, ethnicity, or other socially relevant groupings.
Population characteristics	Human peripheral blood mononuclear cell (PBMC)-derived monocytes were provided by Human Immunology Core of the University of Pennsylvania, isolated from the of healthy volunteers, aged 16 to 64.
Recruitment	The healthy donors were recruited in the Hosptical of the University of Pennsylvania. The written informed consent was obtained from each participant.
Ethics oversight	The collection of human tissues (blood) in compliance with the tissue banking protocol was approved by the University of Pennsylvania Institutional Review Board.

Note that full information on the approval of the study protocol must also be provided in the manuscript.

Field-specific reporting

Please select the one below that is the best fit for your research. If you are not sure, read the appropriate sections before making your selection.

☒ Life sciences ☐ Behavioural & social sciences ☐ Ecological, evolutionary & environmental sciences

For a reference copy of the document with all sections, see nature.com/documents/nr-reporting-summary-flat.pdf

Life sciences study design

All studies must disclose on these points even when the disclosure is negative.

Sample size	The sample size was chosen in advance based on common practice of the described experiments in the literature and our previous work (PMID: 32102932 and 27043280). Sample sizes for comparisons also followed Mead's recommendations. At least 3 of samples per group for all in vitro and in vivo experiments.
Data exclusions	No data was excluded.
Replication	Technical replicates and independent experiments were performed to verify reproducibility of the assays. The replication information is provided in the figure legends.
Randomization	In cell culture experiments, cell dishes were randomly assigned to different study group. In animal studies, all mice used were age- and gender-matched, and were randomly selected.
Blinding	Blinding was not carried out in cell culture experiments or in data collection, in which all experiments had to be carried out by the same researchers. In animal studies, investigators were not blinded, as all primary tissues from which subsequent samples were derived were labeled by genotypes or treatment ways. Blinding was not necessary since measurements did not involve bias from the experiments. All data were processed using the same software.

Reporting for specific materials, systems and methods

We require information from authors about some types of materials, experimental systems and methods used in many studies. Here, indicate whether each material, system or method listed is relevant to your study. If you are not sure if a list item applies to your research, read the appropriate section before selecting a response.

Materials & experimental systems

n/a	Involved in the study
☐	☒ Antibodies
☐	☒ Eukaryotic cell lines
☒	☐ Palaeontology and archaeology
☐	☒ Animals and other organisms
☒	☐ Clinical data
☒	☐ Dual use research of concern
☒	☐ Plants

Methods

n/a	Involved in the study
☒	☐ ChIP-seq
☐	☒ Flow cytometry
☒	☐ MRI-based neuroimaging

Antibodies

Antibodies used

anti-CD3ε (final concentration 1 µg/ml, BioLegend, 100302, Clone 145-2C11) for T cell stimulation
anti-CD28 (final concentration 1 µg/ml, BioLegend, 102102, Clone 37.51) for T cell stimulation
anti-CD3 (1:100, BioLegend,100203/100233, Clone 17A2) for flow cytometry
anti-CD4 (1:100, BioLegend, 100540, Clone RM4-5) for flow cytometry
anti-CD8a (1:100, BioLegend, 100706/100708/100733, Clone 53-6.7) for flow cytometry
anti-CD45 (1:200, BioLegend, 103134/103133, Clone 30-F11) for flow cytometry
anti-F4/80 (1:200, BioLegend, 123107, Clone BM8) for flow cytometry
anti-CD206 (1:100, Biolegend, 141719, Clone C068C2) for flow cytometry
anti-CD80 (1:100, BioLegend, 104713, Clone 16-10A1) for flow cytometry
anti-CD86 (1:100, Biolegend, 105005, Clone GL-1) for flow cytometry
anti-CD86 (1:100, Miltenyi Biotec, 130-102-604, Clone:PO3.3) for flow cytometry
anti-IFN-g (1:100, Biolegend, 505825, Clone XMG1.2) for flow cytometry
anti-Granzyme B (1:100, Biolegend, 372211, Clone QA16A02) for flow cytometry
anti-Ki67 (1:100, Thermo Fisher, 17-5698-80, Clone SolA15) for flow cytometry
anti-LAG3 (1:100, eBioscience, 11-2231-80, Clone C9B7W) for flow cytometry
anti-LAG3 (1:100, Biolegend, 125225/125209, Clone C9B7W) for flow cytometry
anti-PD-1 (1:100, Biolegend, 135223, Clone 29F.1A12) for flow cytometry
anti-Tim-3 (1:100, Biolegend, 134009, Clone B8.2C12) for flow cytometry
anti-CD11b (1:100, Biolegend, 101206/101212, Clone M1/70) for flow cytometry
anti-CD206 (1:100, Biolegend, 321109, Clone 15-2) for flow cytometry
anti-NK-1.1 (1:100, Biolegend, 156505, Clone S17016D) for flow cytometry
anti-TMEM119 (1:100, Thomas Fisher, 25-6119-80, Clone V3RT1GOsz) for flow cytometry
anti-CD25 (1:100, Biolegend, 101915, Clone 3C7) for flow cytometry
anti-CD25 Antibody (1:100, Biolegend, 302610, clone: BC96) for flow cytometry
anti-GD2 (1:100, Biolgend, 357324, Clone 14G2a) for flow cytometry
anti-arginase-1 (1:500, Santa Cruz, sc-20150, Clone H-52) for immunoblot
anti-GAPDH (1:3,000, Cell Signaling, 5174, Clone D16H11) for immunoblot
anti-GD2 (1:200, BioLegend, 357302, Clone 14G2a) for immunofluorescence

Validation

All antibodies were purchased from commercial sources and have been validated by the vendors. Additional validation has also been given in previous publication with PubMed IDs listed:
anti-CD3ε (BioLegend, 100302) PMID: 32901001, 34822775, 36630913 https://www.biolegend.com/nl-be/products/purified-anti-mouse-cd3epsilon-antibody-28
anti-CD28 (BioLegend, 102102) PMID: 32901001, 33893298, 32434937 https://www.biolegend.com/nl-be/products/purified-anti-mouse-cd28-antibody-117
anti-CD3 (BioLegend,100203) PMID: 28560793, 29456159,30393066, 8293463, 2197981 https://www.biolegend.com/nl-be/products/fitc-anti-mouse-cd3-antibody-45
anti-CD4 (BioLegend, 100540) PMID: 29429633, 30446387, 30076101 https://www.biolegend.com/nl-be/products/percp-cyanine5-5-anti-mouse-cd4-antibody-4230
anti-CD8a (BioLegend, 100706/100733) PMID: 29129787, 29363160, 29777108 https://www.biolegend.com/nl-be/products/fitc-anti-mouse-cd8a-antibody-153
anti-CD45 (1:200, BioLegend, 103134/103133) PMID: 30796225, 28008921, 35046097 https://www.biolegend.com/nl-be/products/brilliant-violet-421-anti-mouse-cd45-antibody-7253
anti-F4/80 (BioLegend, 123107) PMID: 28939843, 29664018, 29070674 https://www.biolegend.com/nl-be/products/fitc-anti-mouse-f4-80-antibody-4067
anti-CD206 (1:100, Biolegend, 141719) PMID: 33278339, 35105806, 33571109 https://www.biolegend.com/nl-be/products/pe-cyanine7-anti-mouse-cd206-mmr-antibody-8631
anti-CD80 (1:100, BioLegend, 104713) PMID: 30595553, 30650377, 22308386 https://www.biolegend.com/nl-be/products/apc-anti-mouse-cd80-antibody-2340
anti-CD86 (1:100, Biolegend, 105005) PMID: 33535045, 26644347, 26880763 https://www.biolegend.com/nl-be/products/fitc-anti-mouse-cd86-antibody-254
anti-CD86 (1:100, Miltenyi Biotec, 130-102-604) PMID: 16709832, 15456701 https://www.miltenyibiotec.com/US-en/products/cd86-antibody-anti-mouse-po3-3.html#conjugate=pe:size=30-ug-in-200-ul
anti-IFN-γ (Biolegend, 505825) PMID: 33271118, 30005826, 33711270 https://www.biolegend.com/nl-be/products/pe-cyanine7-

anti-mouse-ifn-gamma-antibody-5865
anti-Granzyme B (1:100, Biolegend, 372211) PMID: 32195350, 36280674, 36054938 https://www.biolegend.com/nl-be/products/percp-cyanine5-5-anti-humanmouse-granzyme-b-recombinant-antibody-15597
anti-Ki67 (1:100, Thermo Fisher, 17-5698-80) PMID: 35045305, 35241842, 36417858 https://www.thermofisher.com/antibody/product/Ki-67-Antibody-clone-SolA15-Monoclonal/17-5698-80
anti-LAG3 (1:100, eBioscience, 11-2231-80) PMID: 36731891, 35915084, 34446716 https://www.thermofisher.com/antibody/product/CD223-LAG-3-Antibody-clone-eBioC9B7W-C9B7W-Monoclonal/11-2231-82
anti-LAG3 (1:100, Biolegend, 125225/125209) PMID: 30580966, 31031094, 33838102 https://www.biolegend.com/nl-be/products/pe-cyanine7-anti-mouse-cd223-lag-3-antibody-14782
anti-PD-1 (1:100, Biolegend, 135223) PMID: 31350404, 32619407, 29958801 https://www.biolegend.com/nl-be/products/apc-cyanine7-anti-mouse-cd279-pd-1-antibody-9742
anti-Tim-3 (1:100, Biolegend, 134009) PMID: 32860752, 34642245, 31722203 https://www.biolegend.com/nl-be/products/pe-cyanine7-anti-mouse-cd366-tim-3-antibody-13929
anti-CD11b (1:100, Biolegend, 101206/101212) PMID: 31488882, 29777220, 29777220 https://www.biolegend.com/nl-be/products/fitc-anti-mouse-human-cd11b-antibody-347
anti-CD206 (1:100, Biolegend, 321109) PMID: 32210962, 32210962, 30995475 https://www.biolegend.com/nl-be/products/apc-anti-human-cd206-mmr-antibody-2996
anti-NK-1.1 (1:100, Biolegend, 156505) PMID: 34852237 https://www.biolegend.com/nl-be/products/apc-anti-mouse-nk-11-antibody-19843
anti-TMEM119 (1:100, Thomas Fisher, 25-6119-80) PMID: 35705056, 33261619 https://www.thermofisher.com/antibody/product/Tmem119-Antibody-clone-V3RT1GOsz-Monoclonal/25-6119-80
anti-CD25 (1:100, Biolegend, 101915) PMID: 29894690, 33106640, 35040435 https://www.biolegend.com/nl-be/products/pe-cyanine7-anti-mouse-cd25-antibody-13235
anti-CD25 Antibody (1:100, Biolegend, 302610) PMID: 35690062, 36261015, 25994968 https://www.biolegend.com/nl-be/products/apc-anti-human-cd25-antibody-614
anti-GD2 (1:100, Biolgend, 357324) PMID: 22585577, 19339105 https://www.biolegend.com/nl-be/products/apccyanine7-anti-human-ganglioside-gd2-antibody-19352
anti-arginase-1 (1:500, Santa Cruz, sc-20150) PMID: 18824264, 22972923, 17577033 https://datasheets.scbt.com/sc-20150.pdf
anti-GAPDH (1:3,000, Cell Signaling, 5174) PMID: 38168040, 37935976, 38095297 https://www.cellsignal.com/products/primary-antibodies/gapdh-d16h11-xp-rabbit-mab/5174
anti-GD2 (1:200, BioLegend, 357302) PMID: 22585577, 19339105 https://www.biolegend.com/nl-be/products/purified-anti-human-ganglioside-gd2-antibody-8407

Eukaryotic cell lines

Policy information about cell lines and Sex and Gender in Research

Cell line source(s)	GL261 cells were from PerkinElmer.
Authentication	GL261 cells were authenticated by the supplying company. No further authentication was performed.
Mycoplasma contamination	All cell lines have been tested and shown negative for mycoplasma contamination.
Commonly misidentified lines (See ICLAC register)	There were no commonly misidentified cell lines used in this study.

Animals and other research organisms

Policy information about studies involving animals; ARRIVE guidelines recommended for reporting animal research, and Sex and Gender in Research

Laboratory animals	Math1-Cre;SmoM2fl/fl (Rosa-LSL-SmoW539L/YFP) mice were generated by breeding SmoM2fl/fl mice with Math1-Cre mice. Wild-type C57/B6 mice were purchased from Jackson Lab. All animals were housed at room temperature with a 12-hour-light/12-hour-dark cycle in the Association for the Assessment and Accreditation of Laboratory Animal Care-accredited animal facility of the University of Pennsylvania. Relative humidity and temperature were maintained at 30-70% and 68-79 oF. For glioma tumor induction experiments, both female and male eight-week-old mice were used.
Wild animals	The study did not involve wild animals.
Reporting on sex	Half male and half female mice were used.
Field-collected samples	The study did not involve samples collected from the field.
Ethics oversight	All experiments with mice were performed in accordance with a protocol approved by the Institutional Animal Care and Use Committee (IACUC) at the University of Pennsylvania.

Note that full information on the approval of the study protocol must also be provided in the manuscript.

Plants

Seed stocks	N/A
Novel plant genotypes	N/A
Authentication	N/A

Flow Cytometry

Plots

Confirm that:

☒ The axis labels state the marker and fluorochrome used (e.g. CD4-FITC).

☒ The axis scales are clearly visible. Include numbers along axes only for bottom left plot of group (a 'group' is an analysis of identical markers).

☒ All plots are contour plots with outliers or pseudocolor plots.

☒ A numerical value for number of cells or percentage (with statistics) is provided.

Methodology

Sample preparation	Tumors were isolated and subjected to mechanical dissociation with a gentleMACS Dissociator (Miltenyi) and enzymatic digestion with collagenase II and dispase II to obtain single cell suspensions. Macrophages were isolated from mouse bone marrow and human blood, followed by different treatments. Single-cell suspensions were stained with control isotype IgG or fluoresence-conjugated antibody, followed by flow cytometry analysis.
Instrument	Canto II (BD Biosciences)
Software	FlowJo v10 software
Cell population abundance	More than 200 thousand cells were sorted.
Gating strategy	All cells were gated. The gating strategy was shown in Extended Data Figure 1.

☒ Tick this box to confirm that a figure exemplifying the gating strategy is provided in the Supplementary Information.